

“TNOs are Cool”: A survey of the trans-Neptunian region

IX. Thermal properties of Kuiper belt objects and Centaurs from combined *Herschel* and *Spitzer* observations^{★,★★}

E. Lellouch¹, P. Santos-Sanz^{1,2}, P. Lacerda³, M. Mommert⁴, R. Duffard², J. L. Ortiz², T. G. Müller⁵, S. Fornasier¹, J. Stansberry⁶, Cs. Kiss⁷, E. Vilenius⁵, M. Mueller⁸, N. Peixinho^{9,10}, R. Moreno¹, O. Groussin¹¹, A. Delsanti^{1,11}, and A. W. Harris⁴

¹ LESIA-Observatoire de Paris, CNRS, UPMC Univ. Paris 6, Univ. Paris-Diderot, 5 Place J. Janssen, 92195 Meudon Cedex, France
e-mail: emmanuel.lellouch@obspm.fr

² Instituto de Astrofísica de Andalucía (CSIC), Glorieta de la Astronomía s/n, 18008 Granada, Spain

³ Queen’s University, University Rd, Belfast BT7 1NN, UK

⁴ Deutsches Zentrum für Luft- und Raumfahrt (DLR), Institute of Planetary Research, Rutherfordstrasse 2, 12489 Berlin, Germany

⁵ Max-Planck-Institut für extraterrestrische Physik (MPE), Postfach 1312, Giessenbachstr., 85741 Garching, Germany

⁶ Space Telescope Science Institute, 3700 San Martin Drive, Baltimore MD 21218, USA

⁷ Konkoly Observatory, Research Centre for Astronomy and Earth Sciences, Hungarian Academy of Sciences, Konkoly Thege 15-17, 1121 Budapest, Hungary

⁸ SRON, Postbus 800, 9700 AV Groningen, The Netherlands

⁹ Center for Astrophysics of the University of Coimbra, Geophysical and Astronomical Observatory, Almas de Freire, 3040-004 Coimbra, Portugal

¹⁰ Unidad de Astronomía, Universidad de Antofagasta, Avenida Angamos 601, Antofagasta, Chile

¹¹ Aix-Marseille Université, CNRS, LAM (Laboratoire d’Astrophysique de Marseille) UMR 7326, 13388 Marseille, France

Received 10 June 2013 / Accepted 12 July 2013

ABSTRACT

Aims. The goal of this work is to characterize the ensemble thermal properties of the Centaurs / trans-Neptunian population.

Methods. Thermal flux measurements obtained with *Herschel*/PACS and *Spitzer*/MIPS provide size, albedo, and beaming factors for 85 objects (13 of which are presented here for the first time) by means of standard radiometric techniques. The measured beaming factors are influenced by the combination of surface roughness and thermal inertia effects. They are interpreted within a thermophysical model to constrain, in a statistical sense, the thermal inertia in the population and to study its dependence on several parameters. We use in particular a Monte-Carlo modeling approach to the data whereby synthetic datasets of beaming factors are created using random distributions of spin orientation and surface roughness.

Results. Beaming factors η range from values <1 to ~ 2.5 , but high η values (>2) are lacking at low heliocentric distances ($r_h < 30$ AU). Beaming factors lower than 1 occur frequently (39% of the objects), indicating that surface roughness effects are important. We determine a mean thermal inertia for Centaurs/TNO of $\Gamma = (2.5 \pm 0.5) \text{ J m}^{-2} \text{ s}^{-1/2} \text{ K}^{-1}$, with evidence of a trend toward decreasing Γ with increasing heliocentric (by a factor ~ 2.5 from 8–25 AU to 41–53 AU). These thermal inertias are 2–3 orders of magnitude lower than expected for compact ices, and generally lower than on Saturn’s satellites or in the Pluto/Charon system. Most high-albedo objects are found to have unusually low thermal inertias. Our results suggest highly porous surfaces, in which the heat transfer is affected by radiative conductivity within pores and increases with depth in the subsurface.

Key words. Kuiper belt: general – planetary systems – planets and satellites: surfaces – methods: observational – techniques: photometric

1. Introduction

Combined optical and thermal observations provide the most common approach to measuring the size and albedos of unresolved airless solar system bodies. Known as the radiometric method, this technique, which dates back to the 1970s (Allen 1970), has been applied to most families of small bodies, especially main-belt asteroids, near-Earth asteroids, and Jupiter Trojans. Initially limited in number by practical constraints on ground-based observations, thermal observations of

asteroids have quickly expanded to large surveys, such as IRAS in 1983 (2200 objects in 1983, Tedesco et al. 2002), AKARI in 2006–2007 (about 5000 objects, Usui et al. 2013), Warm *Spitzer* ExploreNEO since 2009 (600 near-Earth objects, Trilling et al. 2012), and WISE/NEOWISE in 2009–2010, which observed over 150 000 small bodies at 3.4, 4.6, 12, and 22 μm , including some 100 000 main-belt asteroids (Masiero et al. 2011), over 400 NEOs (Mainzer et al. 2011a), and about 2000 Trojans (Grav et al. 2011).

More distant bodies, such as Centaurs and trans-Neptunian objects (TNOs), have been studied much less, due to their faintness and the increasing confusion due to sky emission in the wavelength range where they emit (peak radiation near 100 μm). Except for a handful of objects measured from ground-based

* *Herschel* is an ESA space observatory with science instruments provided by European-led Principal Investigator consortia and with important participation from NASA.

** Table 3 is available in electronic form at <http://www.aanda.org>

radiometry – and several more from stellar occultation and direct imaging – *Spitzer* (2004–2009) provided the first significant dataset on the size/albedo in the Kuiper belt, with about 60 Centaurs/KBOs published measurements at 24 and/or 70 μm (Cruikshank et al. 2005; Grundy et al. 2005, 2007; Stansberry et al. 2006, 2008; Brucker et al. 2009). Building on these results, an observing program entitled “TNOs are Cool!” (Müller et al. 2009) was initiated on *Herschel* (Pilbratt et al. 2010) to observe 130 objects with the Photodetector Array Camera and Spectrometer (PACS; Poglitsch et al. 2010) operating in three bands at 70, 100, and 160 μm . A small subset (11) of the objects were also observed with the Spectral and Photometric Imaging Receiver (SPIRE; Griffin et al. 2010) at 250, 350 and 500 μm . Results for about 75% of the observed sample have been or are being published (Müller et al. 2010; Lim et al. 2010; Lellouch et al. 2010; Santos-Sanz et al. 2012; Mommert et al. 2012; Vilenius et al. 2012; Pål et al. 2012; Fornasier et al. 2013; Kiss et al. 2013a and in prep.; Vilenius et al. 2013; Duffard et al. 2013).

Beyond the measure of sizes and albedos, multi-wavelength thermal radiometry provides information on the surface temperature distribution, as the latter impacts the shape of the emitted spectral energy distribution (SED), i.e. the objects’ color temperature. In addition to the heliocentric distance, Bond bolometric albedo and bolometric emissivity, that together define the mean surface temperature, the temperature distribution is determined by the object’s rotation state (rate and spin-vector orientation), thermal inertia, and surface roughness. The thermal inertia is usually the physical quantity of interest. However, in many cases, the problem is under-determined, as the other parameters involved, particularly the rotational parameters, are poorly or not constrained. Therefore, a simple and powerful approach is to describe the temperature distribution across the object as similar to that resulting from instantaneous equilibrium of a smooth spherical surface with solar radiation (the “equilibrium” (EQM) model), but modified by a “beaming factor” (η) so that the temperature at solar incidence i is given by

$$T = T_{\text{SS}}(\cos i)^{1/4} \quad \text{for } i \leq \pi/2 \quad (1)$$

where the subsolar temperature T_{SS} is given by:

$$T_{\text{SS}} = \left(\frac{F_{\odot} \cdot (1 - A)}{r_{\text{h}}^2 \cdot \eta \cdot \epsilon_{\text{b}} \cdot \sigma} \right)^{1/4} \quad (2)$$

where F_{\odot} is the solar flux at 1 AU, r_{h} is the heliocentric distance in AU, $A = p_{\text{V}} \cdot q$ is the bolometric albedo, and ϵ_{b} is the bolometric emissivity, often assumed to be 0.9. Here p_{V} is the geometric albedo and q is the phase integral, and σ is Stefan-Boltzmann’s constant. The beaming factor is then adjusted to fit the shape of the SED; in essence, by varying the instantaneous equilibrium temperature it enables the model to be matched to the color temperature of the object, as determined from multi-wavelength thermal measurements. More accurate η estimates can be derived if the measurements sample a broader fraction of the SED, and in particular cover both sides of the peak of the Planck function. This approach was originally developed for near-Earth objects (NEOs) – the NEATM model (Harris 1998) – but is applicable to all atmosphereless bodies, and it has been amply demonstrated (e.g. Harris 2006, and references therein) to be vastly superior to EQM (or to models with fixed η , such as the asteroid standard model (STM) which has $\eta = 0.756$; Lebofsky & Spencer 1989) for the purposes of deriving accurate diameters/albedos. In the case of Centaurs/TNOs,

the method was first presented by Stansberry et al. (2008) under the name of “hybrid-STM”, using *Spitzer*/MIPS measurements at 24 and 70 μm . Although strictly speaking the hybrid-STM assumes zero phase angle, while NEATM handles non-zero phase angles, this is unimportant in the case of distant objects¹, and the above papers analyzing *Herschel* data have used equivalently both versions. Throughout this paper we ignored phase angle effects, i.e. did not make the distinction between NEATM and “hybrid-STM”. In principle, therefore NEATM solves for three parameters (diameter, albedo and beaming factor) by fitting at least thermal measurements from at least two bands², with the optical magnitude H_{V} providing a third relation between diameter and albedo (Russell 1916).

The beaming factor is thus a proxy for all combined effects causing a departure of the surface temperatures from the case of a smooth spherical surface in instantaneous equilibrium with insolation³. These include surface roughness and thermal inertia effects, which tend to increase and decrease, respectively, the surface temperatures. In a general sense, “high” η values indicate high thermal inertias, while values less than unity can occur only in presence of surface roughness. Although, for a given object, a physical interpretation of the η -value requires a knowledge of the spin state, the distribution of η values within a population allows one to draw conclusions about the ensemble-averaged thermal inertia of the targets. Such a statistical approach has been demonstrated in the case of near-Earth asteroids by Delbo’ et al. (2007), who inferred a mean thermal inertia for km-sized NEAs of $200 \pm 40 \text{ J m}^{-2} \text{ s}^{-1/2} \text{ K}^{-1}$ (hereafter MKS). In the case of Centaurs/TNOs, the *Spitzer* measurements have provided about 30 beaming factor values, indicating a mean value of $\eta = 1.2$ (Stansberry et al. 2008), but with large scatter due to the large error bars on the individual measurements, and possibly due to a range of spin orientations, spin rates and thermal characteristics. No interpretation of this mean η was presented by Stansberry et al.

In this paper, we take advantage of the broader wavelength coverage and larger sample afforded by the combined *Spitzer*–*Herschel* dataset to conduct a study of the thermal properties of Centaurs/TNOs, sampling the various population subclasses. Section 2 describes the data set. Section 3 describes the modeling approach. Inferences on thermal inertia are presented in Sect. 4 and discussed in Sect. 5.

2. The dataset

We consider a set of 85 Centaurs/TNOs for which *Herschel*/*Spitzer* observations permit a determination of the beaming factor. This includes (i) published values of η , (ii) updated values of η based on published fluxes, (iii) new η values determined from yet-unpublished fluxes. Before describing the dataset, we briefly present the *Herschel* sample.

2.1. The *Herschel* Centaurs/TNO sample

The *Herschel* sample consists of 130 Centaurs/TNOs. For the most part, these objects were selected using source knowledge

¹ Even for a 10° phase angle, larger than can occur in the Centaur/TNO region, phase effects reduce fluxes by less than 2% in the region of the Planck function peak (see Table 2 of Harris 1998).

² Five, including 70 μm redundancy, in the case of the combined *Spitzer*/MIPS–*Herschel*/PACS measurements, widely applicable to the data presented in this paper.

³ In principle the temperature distribution across an object also depends on the object’s shape, but this effect cannot be handled, as in general TNOs shapes are unknown.

as of 2009. Flux predictions in the *Herschel*/PACS bands made use of NEATM and were based, whenever possible, on previous individual diameter/albedo results from *Spitzer*. However, in a more general way, flux estimates made use of H_V magnitudes, assuming fixed values of the geometric albedo ($p_V = 0.08$) and beaming factor ($\eta = 1.25$), based on mean results from *Spitzer* (Stansberry et al. 2008). Objects for which flux predictions exceeded a certain threshold – i.e. for which detection with PACS was expected – were retained in the sample.

An object’s brightness, as expressed by H_V , is proportional to $p_V D^2$ where D is diameter. The thermal flux, on the other hand, is essentially proportional to D^2/Δ^2 (where Δ , the observer-centric distance, is approximately equal to r_h for distant objects) times the Planck function at a temperature which scales as $r_h^{-1/2}$ but is mostly independent of p_V . Because of the thermal flux dependence on D^2/Δ^2 , our sample has a selection bias toward larger objects at greater distances. Smaller objects at great distances would not have been included because their predicted fluxes would be too low. This bias is worsened by the discovery bias against finding small objects at greater distances. There is, in addition, a bias toward discovering preferentially high-albedo objects at greater distances. Such objects, under our assumption of the same albedo for all TNOs, would be “interpreted” as having a larger D (leading to a larger predicted thermal flux), and so would be more likely to be included in our sample. As will be seen below, the D vs. r_h bias is clearly visible in our results, and the p_V vs. r_h bias may also be present. In contrast, there is no bias on η , which enters absolute flux predictions in a rather insensitive way and is essentially determined from the shape of the SED.

2.2. Published η values

A large fraction of the observations performed within the “TNOs are Cool!” program on *Herschel* has been published. *Herschel*/PACS measurements of 19 Classical Objects, 18 Plutinos, and 15 scattered-disk/detached objects were presented by Vilenius et al. (2012), Mommert et al. (2012) and Santos-Sanz et al. (2012) respectively. These measurements, combined with *Spitzer* data whenever available, provided diameter/albedo values for these 52 bodies (2 of which were only limits), as well as 30 (12 Classical + 11 Plutino + 7 scattered disk objects (SDO)/detached) η values⁴. Fornasier et al. (2013) presented flux measurements with *Herschel*/SPIRE for 10 objects, that were combined with *Herschel*/PACS and *Spitzer*, providing alternative η values for 9 of them (with one overlapping object – Huya – in Mommert et al. 2012 and another – Salacia – in Vilenius et al. 2012). We adopted the η values of Fornasier et al. (2013), however generally retaining values based on PACS and MIPS only, as the SPIRE fluxes appear affected by emissivity effects at the longest wavelengths. An extended study of the Classical Objects family by Vilenius et al. (2013) led to the addition of 18 objects, of which 9 have had their η values determined with enough accuracy for our purpose. Most recently, Duffard et al. (2013) analyzed *Herschel*/PACS measurements from 14 Centaurs, and again combined them with *Spitzer* (and WISE in some cases) data to determine the η . Those were included as such, as well as previous *Spitzer* results (Stansberry et al. 2008; Brucker et al. 2009) on four objects not observed by *Herschel*. Finally Kiss et al. (2013a) presented a portrait of the newly discovered and yet unclassified object 2012 DR₃₀,

⁴ When the data could not constrain η , a mean $\eta = 1.20 \pm 0.35$ (Stansberry et al. 2008) was adopted to derive diameters and albedos.

including an η measurement based on *Herschel*/PACS and WISE. In total, this makes 64 objects for which we adopted the published diameters, albedos, and beaming factors without any modifications.

2.3. Updated η values

In a number of situations, we used published fluxes but re-derived new or updated values of η , using NEATM. First, this is the case for 4 SDO/detached whose *Herschel* fluxes were presented in Santos-Sanz et al. (2012) but for which the authors did not attempt to infer η values, in the absence of *Spitzer* measurements. Although *Herschel*-only η are admittedly much less accurate, they are still significant and so we derived them here for completeness. Note that for two of these objects (2007 OR₁₀ and 2007 RW₁₀, only H_R magnitudes are available, so the resulting red albedos p_R were converted into p_V following Santos-Sanz et al. (2012) (i.e., assuming a color index $V - R = 0.55 \pm 0.11$ – typical of SDO/detached objects – for 2007 RW₁₀, and a Quaoar-like value, 0.67 ± 0.02 , for 2007 OR₁₀).

In a few cases, independent albedo/size estimates exist from stellar occultation measurements. For those objects, a single thermal measurement is sufficient to derive the beaming factor. Even in the case of multi-thermal wavelength measurements, the diameter/albedo precision afforded by the occultation technique is superior to that of the radiometric method, so using occultation-derived results will lead to an improved determination of the thermal properties. This was done here for Eris and Makemake (and 2002 TX₃₀₀, see below), i.e. running NEATM but with the diameter and albedo fixed to their known values. The case for Makemake is peculiar, as its 24–500 μm SED cannot be fit with a NEATM (nor a thermophysical model) assuming a homogeneous surface; it is suspected that the SED includes a contribution from a dark and warmer component that dominates at the shortest wavelengths (Lim et al. 2010). For this reason, we considered only the SPIRE measurements at 250–500 μm from Lim et al. (2010), and those were modeled with $D = 1430 \pm 9$ km and $p_V = 0.77 \pm 0.02$ (Ortiz et al. 2012). The resulting η value ($2.29^{+0.46}_{-0.40}$, see Table 3) is similar to that found by Lim et al. (2010) for Makemake “bright terrain” (nominally, 1.9). For Eris, we used the 100 and 160 μm fluxes from Santos-Sanz et al. (2012) updated by Kiss et al. (in prep.), and remodeled them using $D = 2326 \pm 12$ km and $p_V = 0.96 \pm 0.04$ (Sicardy et al. 2011). Although the measurements did provide a 70 μm flux, it was not included in the modeling, as being probably affected by Eris’ satellite Dysnomia or by a hot, dark terrain on Eris to a significant degree.

Finally, Pàl et al. (2012) presented *Herschel*/PACS 70/100/160 μm fluxes of two prominent objects, Sedna and 2010 EK₁₃₉, and inferred their diameter and albedo, mostly based on thermophysical analysis. For consistency, we here remodel their published fluxes with our NEATM (as described in Santos-Sanz et al. 2012). More details on the NEATM fits are given in Sect. 2.4.

2.4. New η measurements

In addition to the above objects, we include here 13 “new” bodies, i.e. observed by *Herschel*/PACS within the “TNOs are Cool!” program, but whose measurements have not been reported previously. These include two classical objects (Varuna and 2002 TX₃₀₀, the latter being a Haumea-family member), four Plutinos (1994 TB, Ixion, 2004 TY₃₆₄ and 1998 VG44),

Table 1. *Herschel* color-corrected fluxes at 70, 100 and 160 μm and H_V -magnitudes for the “new” objects presented in this work.

Object	ObsID	Mid-time	r_h [AU]	Δ [AU]	Flux ₇₀ [mJy]	Flux ₁₀₀ [mJy]	Flux ₁₆₀ [mJy]	H_V
Varuna	1342205140/...5190	10-09-27 08:16	43.5317	43.8432	8.3 ± 2.0	12.8 ± 2.0	9.6 ± 3.6	3.760 ± 0.035
(55636)2002 TX ₃₀₀	1342212764/...2802	11-01-17 03:46	41.6809	41.7619	0.9 ± 0.8	1.4 ± 0.8	5.5 ± 2.2	3.509 ± 0.076
(120348)2004 TY ₃₆₄	1342202885/...2945	10-08-12 09:43	39.4873	39.1725	12.8 ± 0.8	12.2 ± 1.4	12.4 ± 1.7	4.520 ± 0.070
(15820)1994 TB	1342213518/...3569	11-01-31 06:22	27.5066	27.6563	<1.05	1.5 ± 1.5	<1.8	7.934 ± 0.354
Ixion	1342227033/...7152	11-08-23 00:00	41.0852	40.7822	22.7 ± 1.2	25.4 ± 1.4	20.5 ± 3.4	3.828 ± 0.039
(33340)1998 VG ₄₄	1342216446/...6559	11-03-21 07:52	29.4064	29.5116	8.0 ± 0.8	9.9 ± 1.2	1.5 ± 1.4	6.670 ± 0.040
(26308)1998 SM ₁₆₅	1342199499/...9622	10-07-01 11:11	37.9847	38.3707	4.1 ± 1.25	4.8 ± 1.8	<4.0	6.023 ± 0.075
(26375)1999 DE ₉	1342223635/...3670	11-07-04 03:39	36.7526	37.0316	10.1 ± 1.1	9.4 ± 1.3	4.1 ± 3.5	5.154 ± 0.046
(119979)2002 WC ₁₉	1342204317/...4437	10-09-12 05:14	42.2869	42.2487	5.8 ± 1.6	8.0 ± 1.8	7.6 ± 1.8	4.880 ± 0.070
(44594)1999 OX ₃	134220559/...0578	11-05-04 05:08	21.5007	21.9481	10.9 ± 0.7	6.7 ± 0.9	6.2 ± 1.1	7.718 ± 0.092
(48639)1995 TL ₈	1342214043/...4165	11-02-11 08:21	44.1223	44.2789	2.1 ± 0.8	2.3 ± 0.8	<2.1	5.290 ± 0.060
Phoebe	1342212481/	11-01-10 16:41	9.5751	9.4804	301.3 ± 9.7	207.3 ± 7.3	113.2 ± 11.2	6.63 ± 0.01^1
Sycorax	1342221837/...1875	11-01-29 07:00	20.0843	20.5195	17.0 ± 1.0	15.3 ± 1.8	5.5 ± 3.2	7.83 ± 0.06^2

Notes. ObsID: *Herschel* ObsID of the first AOR of a sequence of four AORs of two consecutive observations (first visit/follow-on observation), respectively (no follow-on for Phoebe). Mid-time: Mean date and UT time of the observation. r [AU]: heliocentric distance (AU) for the observation date. Δ [AU]: object-*Herschel* distance (AU) for this date. Error bars and upper limits on fluxes are 1σ . The last column gives the H_V magnitude, as compiled in this work (see text for details) or from literature.

References. ¹⁾ Mainzer et al. (2011b); ²⁾ Romon et al. (2001).

three non-Plutino resonant objects (1998 SM₁₆₅, 2002 WC₁₉ and 1999 DE₉) and two SDOs (1999 OX₃ and 1995 TL₈). Finally we include Saturn’s irregular satellite Phoebe and Uranus’ Sycorax, both of which are thought to be captured Centaurs/TNOs.

Details on the observing technique, data reduction, measurement of the object fluxes, and modeling can be found in the previous “TNOs are Cool!” publications, particularly in Santos-Sanz et al. (2012), and only a brief summary is given here. *Herschel*/PACS observations were performed using the scan map mode, whereby the spacecraft is slewed at constant speed (20"/s) along 10 parallel lines, or “legs“, separated by 4”, and in two intersecting scanning directions. Each such scan-map is repeated two to five times, depending on the expected brightness of the objects. Within a single scan map, either the blue-red (70/160 μm) or the green-red channel (100/160 μm) combination is selected. Furthermore each target is visited twice, with identical observations repeated in both visits with a time interval chosen so that the target moves 30–50” between visits. Data are reduced under the HIPE environment⁵, using a two-stage high-pass filtering procedure, producing one image per visit, filter and scan direction. The changing position of the source with respect to the background in the first vs second visit then allows the background in the individual maps to be determined and subtracted and a background-subtracted, combined image to be obtained. More details on the reduction techniques can be found in Kiss et al. (2013b). Fluxes are extracted from aperture photometry, where a priori knowledge of the source position (near the map center) facilitates its identification. The optimum synthetic aperture to measure the target flux is usually taken as 1.0–1.25 times the FWHM of the PSF in the corresponding filter, and photometric uncertainties are estimated from random implantation of artificial sources and attendant statistical photometry. Fluxes along with their error bars are finally color-corrected using a first guess of the object mean temperature (but

the color-correction is only at the few percent level). Observing conditions and fluxes for the *Herschel*/PACS observations are given in Table 1.

Spitzer/MIPS (Rieke et al. 2004) observations of the same objects were used to complement the *Herschel*/PACS data. Out of the 13 objects, some have fluxes published (Stansberry et al. 2008; Brucker et al. 2009) while others are unpublished. Unpublished data have been processed in a similar way as in Stansberry et al. (2008) and Brucker et al. (2009), using the calibration (Gordon et al. 2007; Engelbracht et al. 2007) and color-correction procedure (Stansberry et al. 2007) described in references therein, and photometric uncertainties are being handled in the same manner. Some of the background subtraction techniques used for our *Herschel* data are in fact derived from techniques originally developed for the MIPS data reductions. The previously unpublished fluxes presented here are based on new reductions of the MIPS data, utilizing updated ephemeris positions for the targets. Observing conditions and fluxes for the *Spitzer*/MIPS observations are given in Table 2.

Color-corrected fluxes and their $1-\sigma$ error bars at 23.78 and 71.42 μm (MIPS), and 70, 100 and 160 μm (PACS) were modeled within NEATM to determine best fit values and uncertainties for the objects diameter D , visible geometric albedo p_V and beaming factor η . In this task, a crucial parameter is the absolute H_V magnitude, for which depending on the object, more or less information may be available (ranging from only rough magnitudes compiled from MPC reports to cases with detailed lightcurve and phase curve information), and we proceeded following Santos-Sanz et al. (2012). In NEATM, Eq. (2) requires some form or value for the phase integral, and following the previous studies, we adopted the albedo-dependent expression $q = 0.336 \cdot p_V + 0.479$ (Brucker et al. 2009). Flux upper limits were treated as non-detections (i.e. zero flux) with a $1-\sigma$ error bar equal to the upper limit. Uncertainties on the three fitted parameters were estimated using the Monte-Carlo method of Mueller et al. (2011), i.e. generating and fitting 1000 synthetic datasets, and adopting the median and the central 68.2% of the solutions. When fits were “bad”, i.e. characterized by a reduced χ^2 significantly larger than 1, we “inflated” the measurement error bars to

⁵ HIPE is a joint development by the *Herschel* Science Ground Segment Consortium, consisting of ESA, the NASA *Herschel* Science Center, and the HIFI, PACS and SPIRE consortia members, see: <http://herschel.esac.esa.int/DpHiPeContributors.shtml>

Table 2. *Spitzer* color-corrected fluxes at 23.68 and 71.42 μm for the “new” objects presented in this work.

Object	Mid-time	r_h [AU]	Δ [AU]	Flux ₂₄ [mJy]	Flux ₇₀ [mJy]	Reference
Varuna	2004-Sep.-22	42.9294	43.2342	0.044 ± 0.035	8.217 ± 2.903	1
(55636) 2002 TX ₃₀₀	2004-Dec.-27	40.7280	40.9780	<0.026	<4.428	1
(120348) 2004 TY ₃₆₄	2007-Aug.-17	39.5979	39.6670	0.145 ± 0.008	7.727 ± 1.312	2
(15820) 1994 TB	2004-Dec.-31	28.3204	28.5620	0.067 ± 0.037	<3.08	1
Ixion	2004-Sep.-27	42.4525	42.7366	0.525 ± 0.041	18.897 ± 5.064	1
(33340) 1998 VG ₄₄	2004-Sep.-24	29.5494	29.8421	0.260 ± 0.070	15.501 ± 3.471	2
(26308) 1998 SM ₁₆₅	2005-Sep.-06	35.9554	36.3023	0.100 ± 0.004	5.403 ± 0.667	1
(26375) 1999 DE ₉	2005-May-14	34.4685	34.9803	0.895 ± 0.084	21.811 ± 3.219	1
(119979) 2002 WC ₁₉	2008-Oct.-25	42.5165	42.7381	0.090 ± 0.009	4.103 ± 0.753	2
(44594) 1999 OX ₃	2004-Oct.-07	24.6652	25.0840	0.630 ± 0.122	2.794 ± 3.323	2
(48639) 1995 TL ₈	2008-Sep.-25	43.3742	43.6947	0.017 ± 0.007	<0.785	2
Phoebe	2005-Apr.-04	9.1012	8.7643	268.4 ± 8.09	402.13 ± 25.60	2

Notes. Mid-time: mean date of the observation. Note that this “mean” value may reflect observations performed several months apart. r [AU]: heliocentric distance (AU) for the observation date. Δ [AU]: distance object-*Spitzer* (AU) for this date. Error bars and upper limits on fluxes are 1σ .

References. ¹⁾ Revised fluxes from [Stansberry et al. \(2008\)](#); ²⁾ previously unpublished data.

Table 4. Correlation results for η values.

Objects	Variables	Number of data points	Correlation coefficient without errors	Correlation coefficient with errors	Significance ²	Confidence ³ level (σ)
All	η vs. r_H	85	0.10	$0.15^{+0.13}_{-0.14}$	0.16	(1.39)
All	η vs. D	85	0.10	$0.18^{+0.13}_{-0.10}$	0.10	(1.64)
All	η vs. p_V	85	-0.19	$-0.06^{+0.15}_{-0.15}$	0.57	(0.56)
All	D vs. r_H	85	0.80	$0.78^{+0.05}_{-0.07}$	<0.000001	(>8.0)
All	p_V vs. r_H	85	0.45	$0.45^{+0.10}_{-0.11}$	0.000014	(4.35)
All	D vs. p_V	85	0.31	$0.30^{+0.12}_{-0.13}$	0.0081	(2.65)
“Good” ¹⁾	η vs. r_H	56	0.15	$0.19^{+0.15}_{-0.16}$	0.17	(1.37)
“Good” ¹⁾	η vs. D	56	0.30	$0.31^{+0.14}_{-0.16}$	0.021	(2.30)
“Good” ¹⁾	η vs. p_V	56	-0.21	$-0.13^{+0.17}_{-0.16}$	0.35	(0.93)
“Good” ¹⁾	D vs. r_H	56	0.87	$0.86^{+0.04}_{-0.06}$	<0.000001	(>8.0)
“Good” ¹⁾	p_V vs. r_H	56	0.34	$0.37^{+0.14}_{-0.16}$	0.0057	(2.78)
“Good”	D vs. p_V	56	0.22	$0.25^{+0.14}_{-0.15}$	0.068	(1.82)

Notes. ⁽¹⁾ Points having η uncertainty <0.3. ⁽²⁾ Significance level of non-correlation. ⁽³⁾ Confidence level of correlation.

obtain more realistic uncertainties, using the procedure and the conditions outlined in [Santos-Sanz et al. \(2012\)](#). For one object of our sample (2002 TX₃₀₀), the diameter and geometric albedo have been measured to be $D = 286 \pm 10$ km and $p_V = 0.088^{+0.15}_{-0.06}$ from stellar occultation ([Elliot et al. 2010](#)). These values were therefore held fixed when running NEATM, with η as the only free parameter.

Phoebe, whose diameter, shape and albedo are known accurately after the *Cassini* measurements, provides a validation of the NEATM approach. It was observed by *Spitzer* (unpublished data, see Table 2), *Herschel*/PACS (Table 1), *Herschel*/SPIRE, and also by WISE ([Mainzer et al. 2011b](#)). In a first step, we used the *Spitzer* and *Herschel*/PACS data to solve for D , p_V , and η . This led to $D = 198 \pm 4$ km and $p_V = 10.4^{+0.3}_{-0.5}\%$. The diameter is only 7% lower than the mean diameter inferred from *Cassini* (213 ± 1.4 km; Thomas 2010). The albedo, on the other hand, is 27% larger than the $0.6 \mu\text{m}$ albedo ($8.2 \pm 0.2\%$) reported from *Cassini*/VIMS by [Buratti et al. \(2008\)](#), a combination of the smaller diameter and probably of the spatial variegation on the

body. Fixing D and p_V to the *Cassini* values, we then inferred $\eta = 1.32^{+0.03}_{-0.047}$ in satisfactory agreement with the WISE value (1.23 ± 0.01). Further analyses of the Phoebe thermal data, including the SPIRE measurements, will be published elsewhere in the context a dedicated thermophysical model.

2.5. Qualitative description of the η results

Results for diameter, geometric albedo, and beaming factor for all objects in our sample (85 objects), including the various sources, are tabulated in Table 3, where the heliocentric distance at the time of observation is also given. In what follows, we focus on the distribution of η values and their variations with other parameters. Results on the size and albedo distributions will be published separately.

Table 4 presents the results of correlation searches between η and the other parameters, using the Spearman-rank correlation coefficients ([Spearman 1904](#)) and following the methods described by Santos-Sanz et al. (2012). In particular, we present correlation coefficients calculated by taking into

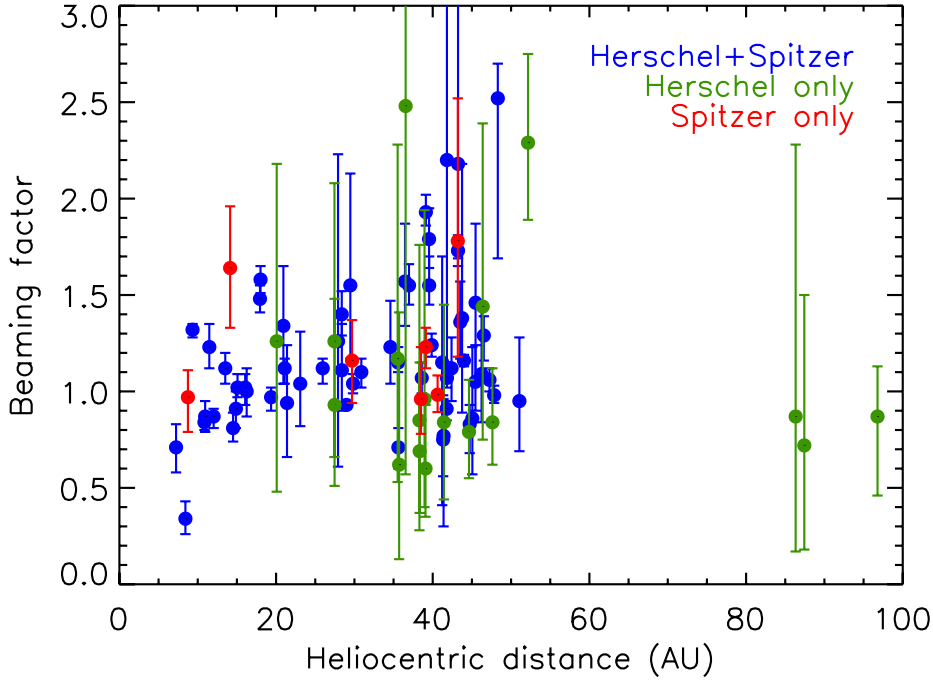


Fig. 1. Observed beaming factor η as a function of heliocentric distance r_h for the entire sample. With two exceptions (objects observed by *Herschel* and WISE, see Table 3), blue (resp. green, red) symbols refer to objects with both *Herschel* and *Spitzer* (resp. only *Herschel*, only *Spitzer*) fluxes.

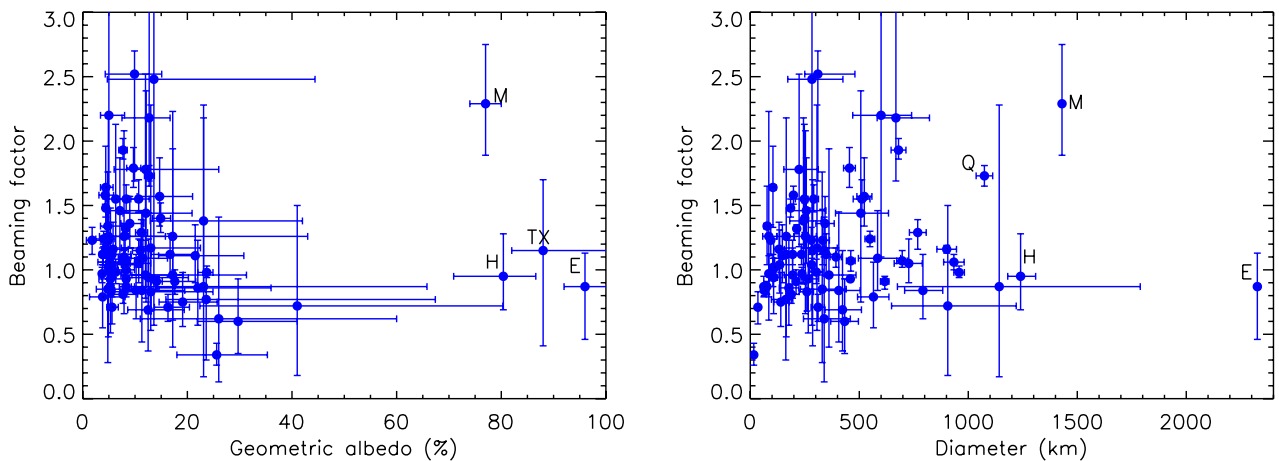


Fig. 2. Beaming factor η as a function of *left*: geometric albedo and *right*: diameter. Labels M, H, TX, E, Q refer to Makemake, Haumea, 2002 TX₃₀₀, Eris and Quaoar, respectively.

account or not the error bars on the parameters. As in the above paper, for the case where error bars are accounted for, Table 4 includes the p -value (i.e. the significance level of no-correlation), and the Gaussian- σ level of the correlation significance. Correlations are calculated on the whole set of 85 objects, and on a reduced set of 56 “good” objects for which the η uncertainty (mean of “upward” and “downward” error bars) is less than 0.3.

Figure 1 shows the derived η factor for all objects as a function of heliocentric distance. A large dispersion of the η values is noticeable, ranging from <1 to ~ 2.5 . A significant fraction of the objects (39%) have central η values lower than 1, indicating important surface roughness effects. The mean value of η is 1.175 if equal weight is given to all objects. When error-bar weighting is applied, a mean value of 1.07 is obtained, close to the median η value (1.09). Note that one object, the Centaur 2005 UJ₄₃₈, exhibits an extremely low η value (nominally <0.5). This could plausibly result from coma activity, as emission of small and

hot particles would enhance the short-wavelength flux, leading to a low apparent η , although Jewitt (2009) did not find any activity on this body. Although a visual inspection of Fig. 1 may suggest a general increase of η with r_h , Table 4 indicates that correlation is weak and only significant at 1.4σ . However, it is noteworthy that within the “core” of the Kuiper belt, i.e. near $r_h = 40$ AU where a large fraction of the sample occurs, the entire $\eta = 0.6$ – 2.5 interval is filled. In contrast, within 30 AU from the Sun, the η values are restricted to progressively narrower ranges, and no objects with $\eta > 2$ are seen at $r_h < 30$ AU, nor with $\eta > 1.5$ at $r_h < 15$ AU. As will be shown, this is an expected behavior for a set of objects with a generally low thermal inertia and a diversity of pole orientations.

Figure 2 shows η as a function of the other two parameters derived from NEATM, i.e. diameter D and geometric albedo p_V . η and D appear to be weakly positively correlated (Table 4), but this may be a consequence of the fact that there is a very strong correlation between r_h and D in our sample (itself a target

Table 5. Adopted rotational properties.

Object	Period (h)	Δm mag	Ref.	Object	Period (h)	Δm mag	Ref.
Chiron	5.9180 ± 0.0001	0.088 ± 0.003	(1)	2005 UJ ₄₃₈	8.32	0.13 ± 0.01	(4)
Amycus	9.76	0.16 ± 0.01	(4)	Asbolus	4.47	0.55	(2, 3)
Bienor	9.14 ± 0.04	0.75 ± 0.09	(5)	Echeclus	13.401	0.24 ± 0.06	(13)
2003 WL ₇	8.24	0.05 ± 0.01	(4)	Okyrhoe	4.86/ 6.08	0.07 ± 0.01	(4)
Pholus	9.98	0.60	(14,15,16)	Thereus	8.3091 ± 0.0001	0.16 ± 0.02	(5)
2002 GZ ₃₂	5.80 ± 0.03	0.15 ± 0.03	(10)	2003 CO ₁	4.51	0.07 ± 0.01	(4)
Teharonhiawako	4.7526 ± 0.0007	0.20	(6)	Makemake	7.65	0.014 ± 0.002	(4)
2004 GV ₉	5.86 ± 0.03	0.16 ± 0.03	(10)	Salacia	6.09 /8.1	0.03 ± 0.01	(4)
Haumea	$3.9154 \pm 0.0001^*$	0.28 ± 0.02	(4)	Varuna	6.3418	0.43 ± 0.01	(4)
2002 AW ₁₉₇	8.87 ± 0.01	0.04 ± 0.01	(7)	Quaoar	17.68 /8.84	0.15 ± 0.04	(4)
2002 UX ₂₅	14.38	0.21 ± 0.06	(13)	2002 TX ₃₀₀	8.16	0.04 ± 0.01	(4)
2003 MW ₁₂	5.90	0.06 ± 0.01	(4)	2004 TY ₃₆₄	11.70 ± 0.01	0.22 ± 0.02	(17)
1999 TC ₃₆	6.21	0.06	(5)	2000 GN ₁₇₁	8.329 ± 0.05	0.61 ± 0.03	(8)
2002 VE ₉₅	9.97	0.05 ± 0.01	(4)	2003 AZ ₈₄	6.78*	$0.10 \pm 0.01^*$	(4)
2003 VS ₂	7.42	0.21 ± 0.01	(4)	2004 UX ₁₀	5.68	0.08 ± 0.01	(4)
Huya	6.75	0.05	(5)	Orcus	10.47	0.04 ± 0.01	(4)
1994 TB	6.50	0.30	(18)	1998 SM ₁₆₅	7.1 ± 0.1	0.45 ± 0.03	(8)
1996 TL ₆₆	12.0	0.07 ± 0.02	(4)	2002 PN ₃₄	10.22	0.18 ± 0.04	(6)
Ceto	4.43 ± 0.03	0.13 ± 0.02	(8)	Typhon	9.67	0.07 ± 0.01	(4)
2003 FY ₁₂₈	8.54	0.15 ± 0.01	(4)	Sedna	10.273 ± 0.003	0.02	(9)
Eris	28.08	0.01	(12)	Phoebe	9.2735 ± 0.0006	0.128 ± 0.006	(19, 20)
Sycorax	3.60 ± 0.02	0.067 ± 0.004	(21)	1999 TD ₁₀	15.382 ± 0.001	0.53 ± 0.03	(22)

References. ⁽¹⁾ Bus et al. (1989); ⁽²⁾ Davies et al. (1998); ⁽³⁾ Kern et al. (2000); ⁽⁴⁾ Thirouin et al. (2010); ⁽⁵⁾ Ortiz et al. (2003); ⁽⁶⁾ Osip et al. (2003); ⁽⁷⁾ Ortiz et al. (2006); ⁽⁸⁾ Sheppard & Jewitt (2002); ⁽⁹⁾ Gaudi et al. (2005); ⁽¹⁰⁾ Dotto et al. (2008); ⁽¹¹⁾ Lacerda & Luu (2006); ⁽¹²⁾ Duffard et al. (2008); ⁽¹³⁾ Rousselot et al. (2005a); ⁽¹⁴⁾ Hoffmann et al. (1992); ⁽¹⁵⁾ Farnham (2001); ⁽¹⁶⁾ Tegler et al. (2005); ⁽¹⁷⁾ Sheppard (2007); ⁽¹⁸⁾ Romanishin & Tegler (1999); ⁽¹⁹⁾ Bauer et al. (2004); ⁽²⁰⁾ Miller et al. (2011); ⁽²¹⁾ Maris et al. (2007); ⁽²²⁾ Rousselot et al. (2005b). * Updated value. In case of multiple values of the period, the one chosen is in boldface.

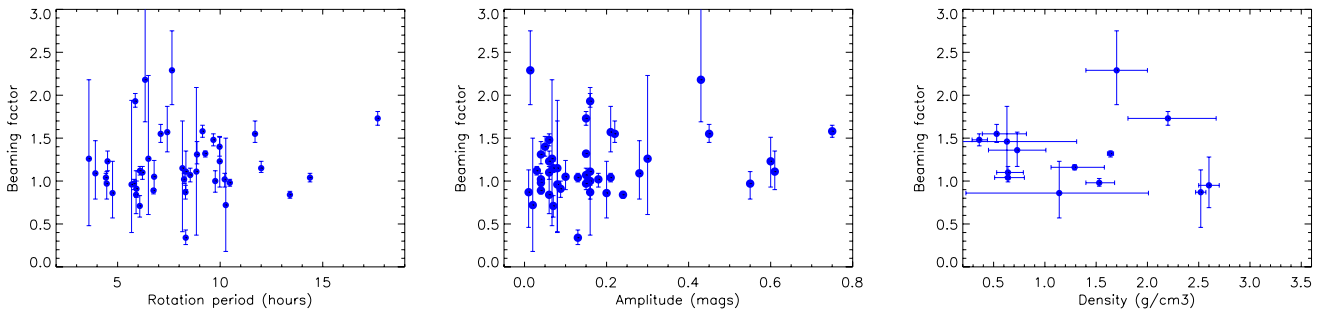


Fig. 3. Beaming factor η as a function of *left*: lightcurve period (44 objects) *middle*: lightcurve amplitude (same 44 objects) and *right*: density (14 objects). Lightcurve information is taken from Table 5 and density values from literature (see text).

discovery/selection bias, as discussed in Sect. 2.1). The η vs. p_V plot indicates that while low-albedo objects explore the full range of η , high-albedo objects tend to have exclusively low- η values. In fact, all objects with geometric albedos higher than 20% have $\eta < 1.5$, with one exception (Makemake). No significant correlation is present beyond $1\text{-}\sigma$ between η and p_V . This result is noticeable in view of the positive correlation (coefficient $+0.45$, 4.3σ) between r_h and p_V in our sample (which may reflect the selection bias discussed in Sect. 2.1). Rotational information (i.e. lightcurve period P and amplitude Δm) is available for 44 objects of the sample, as summarized in Table 5. Density (ρ) estimates are also available for 14 objects, mostly binary systems (Sicardy et al. 2011; Santos-Sanz et al. 2012; Vilenius et al. 2012; Mommert et al. 2012; Ortiz et al. 2012; Fornasier et al. 2013). Figure 3 shows plots of η vs. Δm , P and ρ , none of which shows trends beyond the 1.3σ confidence level.

In what follows, we present models to derive ensemble thermal properties of the population. We mostly focus on the interpretation of the η vs. r_h behavior, but also study the η vs. p_V relationship.

3. Model

3.1. Relating beaming factor to thermal parameter

As indicated in the Introduction, for a spherical object, the beaming factor includes the combined effects of surface roughness and thermal inertia. Thermal inertia effects are not only dependent on the value of the thermal inertia (Γ) but also on the rotation state (i.e. spin orientation and rate) of the object. For a given spin orientation, characterized by the subsolar latitude on the object β (which for distant objects can be assumed identical to the

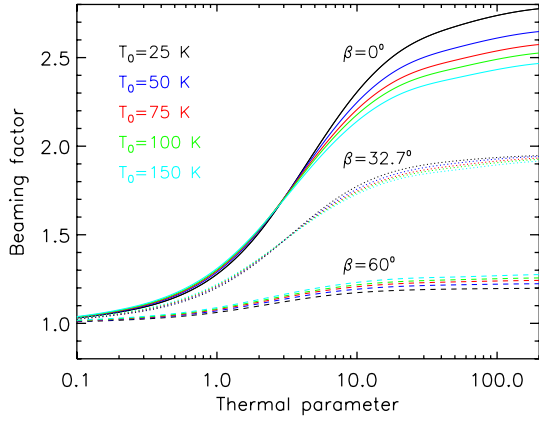


Fig. 4. Model beaming factor η as a function of thermal parameter Θ for three values of the subsolar/subearth latitude β and five values of the instantaneous subsolar temperature T_0 .

subobserver latitude), the degree to which the surface responds to insolation is fully characterized by the so-called “thermal parameter”, Θ (Spencer et al. 1989). Θ is equal to the ratio of the characteristic timescale for radiating heat from the subsurface to the diurnal timescale, and is expressed as:

$$\Theta = \frac{\Gamma \sqrt{\omega}}{\epsilon_b \sigma T_0^3} \quad (3)$$

Here $\omega = 2\pi/P$ is the body rotation rate, where P is the rotation rate, ϵ_b , σ have been defined previously and T_0 is the instantaneous equilibrium subsolar temperature (given as T_{SS} per Eq. (2) but omitting the beaming factor). Objects with the same value of Θ exhibit the same diurnal temperature profile, provided they have the same spin orientation (i.e. β). More generally, local temperatures can be written as (e.g. Lellouch et al. 2000):

$$T = T_0 \times f(\text{latitude, local time, } \beta, \Theta) \quad (4)$$

where $f(\text{latitude, local time, } \beta, \Theta)$ is a temperature function, that depends on the thermal parameter and on local insolation (through latitude, local time, and subsolar latitude); when $\Theta = 0$, $f = 1$ at the subsolar point.

Thus, Θ and β control the temperature distribution at the surface, as does η semi-empirically. The first task is therefore to quantitatively relate η to Θ , for a given value of β . For this we first produced a series of thermophysically-based temperature distributions, entirely defined by the values of T_0 , Θ and β . For each model, and using an object of arbitrary radius, the object-integrated SED was calculated and then refit with NEATM to determine the equivalent value of the beaming factor. In practice, the emitted flux was calculated at the five wavelengths from which most of our observational determinations of η were obtained (i.e. 23.78, 70, 71.42, 100 and 160 μm). As the SED varies drastically in shape with the absolute temperatures, this was performed on a grid of five values of the subsolar temperatures encompassing the range of our measurements, given the heliocentric distances and determined albedos: $T_0 = 25, 50, 75, 100$ and 150 K.

Results are shown in Fig. 4 for the five values of T_0 and three values of β (0° , 32.7° , and 60°). Note that $\beta = 32.7^\circ$ ($=(\pi/2 - 1)$ rad) is the mean value in the case of a uniform distribution of spin orientations on a sphere (in such a distribution, a particular β_i value is weighted by $\cos \beta_i$). Unsurprisingly, results are strongly dependent on β . In contrast the $\eta(\Theta)$ relation is

much less dependent on T_0 . This will permit us, for a particular object, to interpolate between the various T_0 curves. Note that when $\beta = 90^\circ$ (not shown in Fig. 4), $\eta = 1$ for any Θ value, as the temperature distribution on a smooth sphere with pole-on orientation is identical to the instantaneous equilibrium case, regardless of thermal inertia.

3.2. Surface roughness effects

Figure 4 shows that in the limit of high values of the thermal parameter, the beaming factor reaches asymptotic values of 2.5–2.8 for equator-on orientations ($\beta = 0^\circ$). This is consistent with the highest η values in our observational sample (e.g. Fig. 1). However, the data also indicate a number of $\eta < 1$ cases, not accounted for in Fig. 4. These are due to surface roughness effects, not included in the previous section.

Surface roughness is usually treated in models by adding craters of variable opening angle and surface coverage on a smooth sphere, and by accounting for shadowing and multiple scattering of solar and thermal radiation as well as heat conduction inside craters (Spencer 1990; Lagerros 1996; Emery et al. 1998; Delbo’ et al. 2007; Davidsson et al. 2009). These models for the most part have been applied to unresolved asteroid observations. More recently, Rozitis & Green (2011) presented models describing the observed directional thermal emission from any atmosphereless planetary surface. In addition to the description in terms of the above two crater parameters, roughness can also be parameterized in terms of the mean surface slope angle ($\bar{\theta}$, Hapke 1984; Emery et al. 1998), or the rms surface slope (s , as defined by Spencer 1990), or the rms surface “roughness” (ρ , defined by Lagerros 1998).

The work by Spencer (1990) is appropriate to our study as it directly links surface roughness to the beaming factor η of the NEATM. In particular, he showed that the effect of a roughness level s can be seen as a “negative” contribution to η , such as $\delta\eta(\Theta, s) = \eta(\Theta, s) - \eta(\Theta, 0)$. The most important feature of $\delta\eta$ is that it is a function of Θ ; in particular $\delta\eta$ decreases with Θ and converges to ~ 0 at $\Theta > 30$. This can be explained by temperature profiles within craters becoming progressively isothermal at high values of Θ . Otherwise $\delta\eta$ is to high accuracy constant with subsolar latitude β , and also largely independent of wavelength (especially longward of the Planck maximum).

Here we considered two of the roughness cases described by Spencer (1990): (i) the 50% coverage, 90° opening angle case, which we termed “moderate roughness” (ii) the 100% coverage, 90° opening angle case, a maximum roughness situation which we called “high roughness”. The two cases respectively give $\delta\eta = 0.24$ and $\delta\eta = 0.38$ at $\Theta = 0$, decreasing with the thermal parameter. They approximately correspond to rms surface roughness $\rho \sim 0.6$ and ~ 0.9 , respectively, in the formalism of Lagerros (1998; see his Fig. 2).

Implementing the $\delta\eta(\Theta)$ corrections as per Fig. 6 of Spencer (1990), Fig. 5 shows the beaming factor vs thermal parameter relationship with and without surface roughness, for four values of β , restricting ourselves to the $T_0 = 50$ K for figure clarity. The presence of surface roughness allows us to account for low η values in the low Θ regime, down to a minimum of $\eta = 0.62$ for high roughness and $\eta = 0.79$ for moderate roughness, while high η values are maintained for high Θ (up to ~ 2.6 for $\beta = 0^\circ$ and 1.95 for $\beta = 32.7^\circ$). Overall this behavior accounts for the majority of the observationally-derived η ’s. Figure 5 also shows that for a given orientation, the interpretation of a particular η value depends on the assumed roughness scenario, illustrating the roughness/thermal parameter degeneracy.

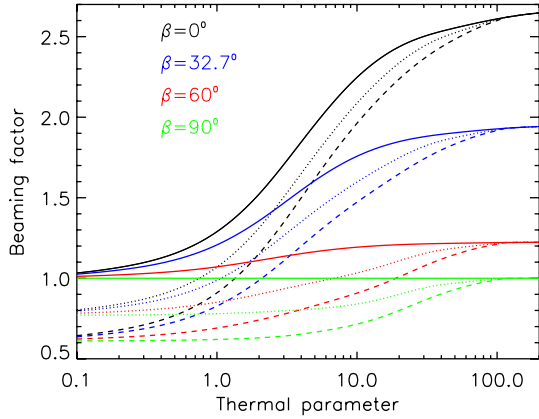


Fig. 5. Model beaming factor η as a function of thermal parameter Θ for four values of the subsolar/subearth latitude β and three surface roughness levels: Solid line: no roughness. Dotted line: moderate roughness. Dashed line: high roughness. The instantaneous subsolar temperature T_0 is 50 K.

4. Thermal inertia results

4.1. Fixed spin state and roughness

With the above model, we now invert the measured η in terms of individual values of the thermal inertia. For this, in a first step, we assume that all objects have the same spin orientation, spin rate and surface roughness. For spin orientation, we consider both $\beta = 32.7^\circ$ and $\beta = 0^\circ$. As representing a more likely mean orientation of the population, the first value is preferred. Admittedly, $\beta = 0^\circ$ permits an easier fit of high (>1.95) η values, but given the error bars, there is no unambiguous evidence for such values in our sample. We consider both the “high roughness” and “moderate roughness” cases, preferring the first case given the lowest measured η values. For a given (β , roughness) scenario, the measured η are solved in terms of the thermal parameter Θ (interpolating between the relevant T_0 curves – see Fig. 4 – where T_0 is calculated for each object from its heliocentric distance and albedo). Θ is finally converted to the thermal inertia Γ using Eq. (3), assuming a rotation period $P = 8$ h, a reasonable representative value for the TNO / Centaur population (see Fig. 3). Note that as Γ/Θ depends only weakly (power 1/2) on P , the uncertainty on P for a given object has not a large impact.

Results are summarized in Fig. 6 for the four cases. Considering the nominal η values, i.e. not accounting for error bars, the model gives Θ solutions for 70–82 objects out of 85 (i.e. 82–96%), depending of the (β , roughness) case (for the remaining 3–15 objects, the nominal η values cannot be fit by the model). Moreover 66–78 objects (i.e. 78–92%) have thermal inertia Γ less than $20 \text{ J m}^{-2} \text{ s}^{-1/2} \text{ K}^{-1}$ (MKS), and 45–63 objects (53–74%) have $\Gamma < 5$ MKS. For the four considered cases, the median value of Γ varies from 1.7 MKS ($\beta = 0^\circ$, moderate roughness) to 4.2 MKS ($\beta = 32.7^\circ$, high roughness). For a given orientation, the ratio of the “high roughness” to the “moderate roughness” thermal inertia is in the range 1.3–1.8 for most objects, illustrating the well-known partial degeneracy between thermal inertia and roughness properties in defining the thermal fluxes. Overall, the distribution of η is indicative of a low thermal inertia for most objects. All four cases of Fig. 6 give the visual impression of a decrease of thermal inertia with increasing heliocentric distance. This is confirmed by simple Spearman rank correlation calculations (i.e. not including error bars on Γ). The strongest correlation between Γ and r_h

is found for the ($\beta = 32.7^\circ$, high roughness) case (coefficient: -0.58 ; 5.0σ confidence), while the least significant is obtained for the ($\beta = 0^\circ$, moderate roughness) case (coefficient: -0.40 ; 3.5σ). Fitting the (r_h, Γ) values with a power-law function in the form $\Gamma(r_h) = \Gamma(30 \text{ AU}) \times (r_h/30)^{-\alpha}$ (accounting for error bars) yields a power exponent α in the range 1.40–1.94 for the various orientation, roughness cases, and $\Gamma(30 \text{ AU}) = 2.0$ – 4.0 MKS. Hence this analysis suggests a rapid decrease of thermal inertia with increasing heliocentric distance over 8–50 AU where most of the measurements refer to.

For the mean $\beta = 32.7^\circ$ orientation and the two roughness cases, Fig. 7 shows the inferred thermal inertia as a function of geometric albedos. The data indicate a general trend of a decrease of Γ with increasing p_V . The noted absence of high values of η for bright objects (see Fig. 2) translates into a lack of “high” Γ values (>5 MKS) for objects having p_V higher than $\sim 20\%$. The Spearman correlation coefficient between Γ and p_V is -0.47 and -0.35 for the high and moderate roughness cases, with 4.0 and 2.9σ significance respectively. For the $\beta = 0^\circ$ case (not shown in Fig. 7), the significance of a decrease of Γ with p_V is of 3.6 and 2.6σ for the two roughness cases, respectively. Note that this moderate Γ vs. p_V anticorrelation can also be seen as an anticorrelation (with similar magnitude and significance) between Γ and diameter. In fact, geometric albedo and diameter in our sample appear to be positively correlated at 2.6σ (see Table 4), and a (Γ , diameter) plot shows a lack of Γ values higher than 5 MKS for objects larger than ~ 700 km in diameter, with Quaoar and Makemake as exceptions.

4.2. Attempting to use rotational information

As indicated above, rotational information (i.e. lightcurve period P and amplitude Δm) is available for 44 objects of the sample. In a first step, we used the actual P of these objects to invert η in terms of Γ , still keeping the assumption of fixed orientation and roughness. Results are shown in Fig. 8 for the same four cases as in Fig. 6, but this time plotted as a function of rotational period. Similar to Fig. 6, and noting also that error bars are usually smaller for points with lower thermal inertia, the figure indicates low thermal inertia, with median values ranging from 2.0 MKS ($\beta = 0^\circ$, moderate roughness) to 4.5 MKS ($\beta = 32.7^\circ$, high roughness). Although Fig. 8 might visually suggest an increase of the thermal inertia with rotation period, the Spearman rank correlation indicates that such a correlation is not significant beyond the 1.0 – 1.6σ level, depending on the (β , roughness) case.

The above analyses are still limited by the unknown orientation (β). We attempted to further use rotational information by assuming that objects exhibiting a sufficiently marked lightcurve adopt Jacobi equilibrium figures, i.e. are ellipsoids with $a > b > c$ axes. In this case, the shape (i.e. the axis ratios) is defined by the rotation period and density, and the lightcurve amplitude then defines the viewing angle (β). Specifically, upon an assumption on the object density (ρ), we used the rotation period $P = 2\pi/\omega$ to calculate $\omega^2/(\pi G \rho)$, where G is the gravitational constant. When lower than a limit of 0.3742, the latter quantity provides c/a and b/a by interpolation from Chandrasekhar’s (1987) tables (see also Lacerda & Jewitt 2007). We considered two density cases ($\rho = 1000$ and 3000 kg m^{-3}) and restricted ourselves to objects with some minimum lightcurve amplitude (Δm_{\min}), considering that lightcurves with lower amplitudes may instead be due to albedo markings on a MacLaurin spheroid. Once c/a and b/a are known, β was determined from equations given e.g. in Lacerda & Luu (2003) or Rabinowitz et al. (2006)

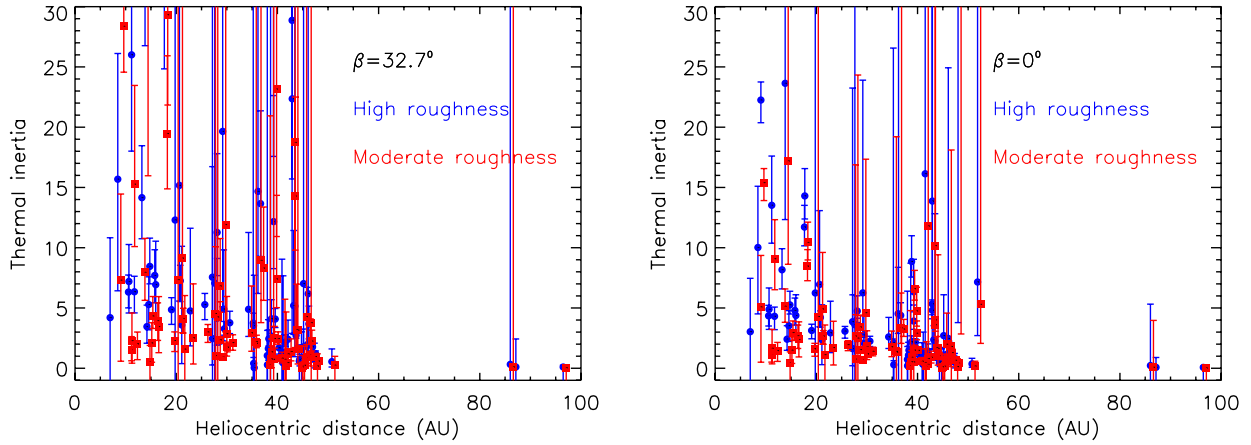


Fig. 6. Individual thermal inertia vs. heliocentric distance, as inferred from the measured η for two values of the subsolar latitude ($\beta = 32.7^\circ$ and 0°) and the two surface roughness cases (“high” and “moderate”).

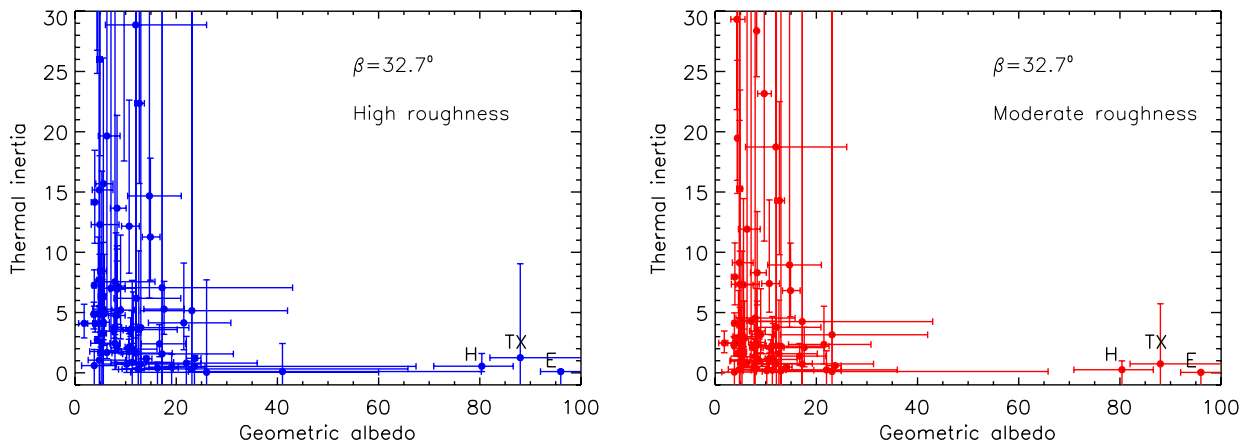


Fig. 7. Individual thermal inertia vs. geometric albedo, as inferred from the measured η for a subsolar latitude $\beta = 32.7^\circ$ and the two surface roughness cases. Labels H, TX and E refer to Haumea, 2002 TX₃₀₀, and Eris, respectively.

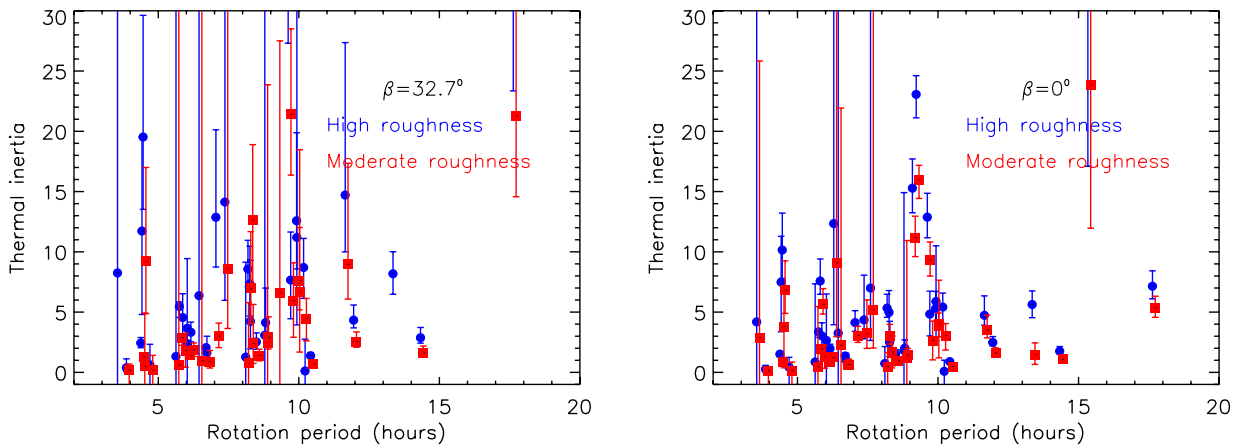


Fig. 8. Individual thermal inertia for 44 objects as a function of rotational period, as inferred from the measured η , for two values of the subsolar latitude ($\beta = 32.7^\circ$ and 0°) and two cases of surface roughness (“high” and “moderate”).

(page 1250, with $\beta = 90^\circ - \Phi$). The conversion of the beaming factors to thermal inertia was then performed using the individual values of P and β , again considering the “moderate” and “high” roughness cases.

This approach was only moderately successful. We started with $\Delta m_{\min} = 0.10$. This case leads to solutions in terms of Γ for only 13 (for $\rho = 1000 \text{ kg m}^{-3}$) to 18 objects (for $\rho = 3000 \text{ kg m}^{-3}$). Results, shown in Fig. 9, indicate somewhat more dispersed and higher Γ values than before. This mostly

results from the fact that the mean values of β deduced from the Jacobi equilibrium assumptions (47° and 50° for $\rho = 1000$ and 3000 kg m^{-3} respectively) are higher than those considered before for the population as a whole (0° and 32°). The median values of the thermal inertia, very similar for the two density cases, are typically 5–7 MKS and 17–23 MKS for the moderate and high roughness cases. However, we are not inclined to trust the results too much, especially because of the high β values, even higher than would be produced by a random distribution

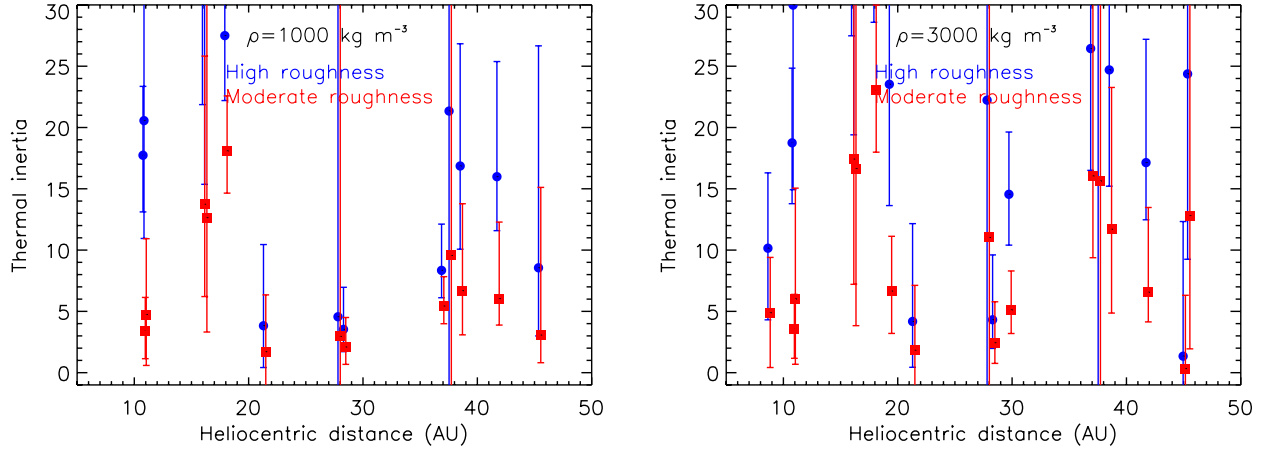


Fig. 9. Individual thermal inertia for objects having rotational lightcurve amplitudes $\Delta m > 0.10$, using subsolar latitudes estimated from the assumption of Jacobi equilibrium figures, using two values of the density (1000 and 3000 kg m^{-3}), and two cases of surface roughness (“high” and “moderate”).

of polar axes in the ecliptic plane (leading to a mean β of 45°). This probably means that $\Delta m_{\min} > 0.10$ is not strict enough to isolate the Jacobi ellipsoids, which is supported by the conclusion of Duffard et al. (2009) that the majority of large TNOs are in fact MacLaurin spheroids, with a relative fraction increasing from 30% at low density ($\rho = 500 \text{ kg m}^{-3}$) to more than 90% for $\rho = 2500 \text{ kg m}^{-3}$. Using a more restrictive $\Delta m_{\min} = 0.20$ criterion, only 7–10 objects have Γ solutions, with (still high) mean β values of 38° and 42° for $\rho = 1000$ and 3000 kg m^{-3} , and median values of Γ of 3–5 MKS and 8–17 MKS for the moderate and high roughness cases, respectively.

4.3. Monte-Carlo simulations

In a second, somewhat less model-dependent approach, we calculated “synthetic” datasets under various assumptions and compared them to the observed distribution of beaming factors. In practice, we generated a family of objects characterized by their individual heliocentric distance, spin orientation (β) and surface roughness. In general we assumed all objects to have a fixed rotation period $P = 8$ h and a fixed geometric albedo of $p_V = 0.1$. As discussed above, results on the thermal inertia are relatively insensitive to P , and except for high-albedo objects, also rather insensitive to p_V (through T_0 , see Fig. 4). In contrast, as is obvious from Fig. 5, they are strongly dependent on β and surface roughness, which were handled as follows. For each object of the simulation, a β value was randomly generated. We nominally assumed a uniform distribution of the spin axes orientations on the sphere. As discussed below, an alternative distribution of spin axes was also tested. For surface roughness, we considered the three cases (“no roughness”, “moderate roughness” and “high roughness”) previously described, assuming that they apply to all objects of the family (“fixed roughness cases”). In addition, we considered a so-called “random roughness” scenario, in which for each object, a roughness level was assigned randomly – considering a uniform distribution between the no-roughness and high roughness limiting cases. In the model and for any of the three “fixed roughness” cases, the distribution of β values is responsible for the diversity of η values at a given heliocentric distance r_h , and the η distribution is further broadened in the random roughness scenario.

Comparison to the data was performed by using the two-dimensional Kolmogorov-Smirnov test (e.g. Press et al. 1992).

For each observed object, we calculated a set of 100 artificial objects having the same observed r_h , but random values of β (and roughness, for the latter scenario). The model was then run for a series of values of the thermal inertia Γ in the range 0.5–50 MKS. The fit quality was then assessed from the Kolmogorov-Smirnov (K-S) distance d in the (r_h, η) plane. In essence, this distance quantifies the extent to which two 2-D datasets are similar (the more similar they are, the smaller d is). The K-S test also returns a significance level p_{KS} for the fact that the two datasets derive from different distributions (the smaller p_{KS} , the more different the distributions are likely to be).

For each model distribution, the K-S test was run by using the nominal (i.e. central) values of the measured η , providing the K-S distance $d(\Gamma)$, and therefore the best fit value for Γ , noted Γ_0 . In addition, the sensitivity of the results to the measurement uncertainties was assessed by varying the measured η values within their error bars (using normally distributed random noise at the level indicated by the measurements). This was done for 100 repetitions, each of which returned a value of Γ_0 , finally providing the mean value of Γ_0 and its standard deviation. Overall, the approach is similar to that adopted by Delbo’ et al. (2007) for determining the thermal inertia of near-Earth asteroids, except that they analyzed the behavior of η vs. phase angle instead of η vs. r_h .

Results for $d(\Gamma)$ are shown in the left panel of Fig. 10 for the four considered cases. This panel shows that with a minimum d value of 0.35 (corresponding to $p_{KS} = 6 \times 10^{-7}$ at best fit), the no-roughness case can be rejected. For comparison, the “high”, “moderate” and “random” roughness cases have similar minimum d of 0.15–0.18, i.e. p_{KS} in the range 0.06–0.09. The right panel of Fig. 10 shows histograms of the best fit Γ_0 values when measurement uncertainties are considered. Excluding the no-roughness case, the solution ranges of Γ_0 values are (3 ± 0.7) MKS, (5 ± 0.5) MKS and (2.5 ± 0.5) MKS for the moderate, high and random roughness cases, respectively. This range of values is in general agreement with inferences from the first approach (Sect. 4.1).

For our preferred “random roughness” case, Fig. 11 presents the model-calculated η vs r_h distribution, for three values of Γ (1, 2.5 and 8). Here 750 points have been generated randomly in the manner explained previously, except that for a better visualization, a regular grid in r_h in the 5–50 AU range has been adopted instead of retaining the measurements r_h . For a given Γ value,

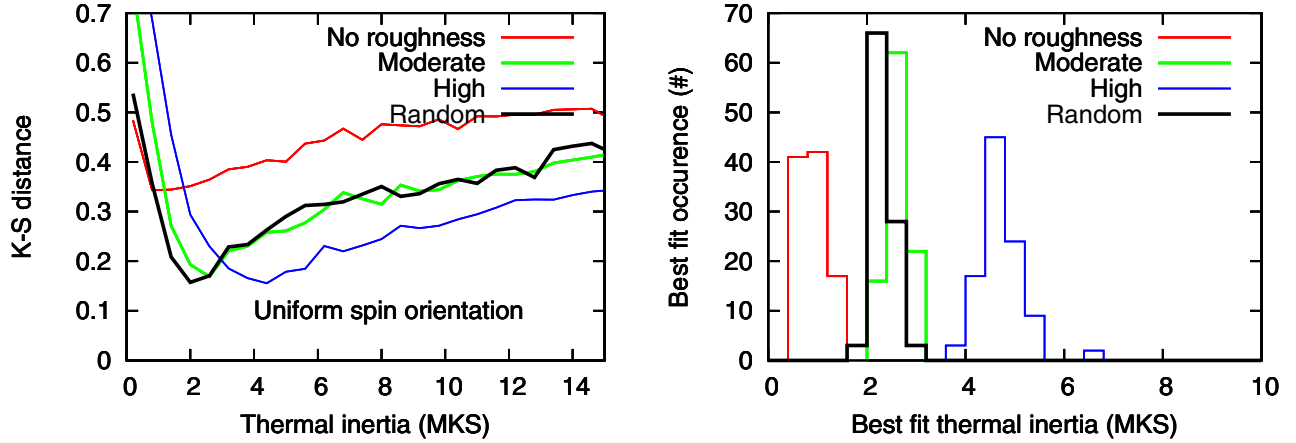


Fig. 10. *Left:* Kolmogorov-Smirnov distance d between the observed distribution of η and those calculated as a function of thermal inertia for the four roughness scenarios. In all cases, a uniform distribution of the polar axes over the sphere is assumed. The minimum of d indicates the best fit thermal inertia Γ_0 . *Right:* histograms showing the distribution of best fit Γ_0 , when accounting for uncertainties in the η measurements (see text).

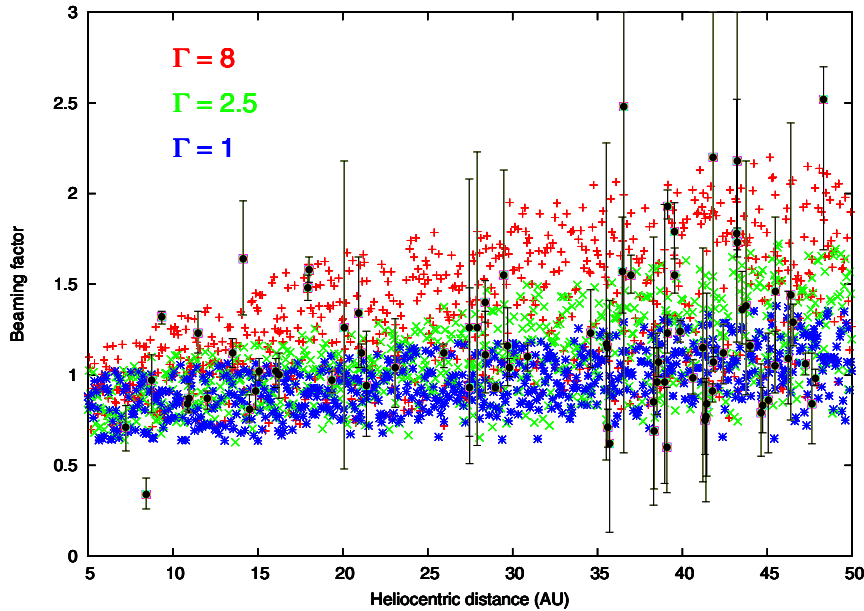


Fig. 11. Beaming factor η as a function of heliocentric distance r_h for the entire sample, compared with Monte-Carlo simulations assuming a rotation period of 8 h, a geometric albedo of 0.1, a uniform distribution of the polar axes on the sphere, and a random distribution of surface roughnesses. Thermal inertia $\Gamma = 1, 2.5$ and 8 MKS cases are shown here. Although $\Gamma = 8$ MKS may seem needed to account for the three points with $\eta = 1.5$ –1.8 at 13–18 AU, this case underpredicts the number of low η values at $r_h > 25$ AU, and $\Gamma = 2.5$ MKS provides the overall best fit.

the general increase of η with r_h is simply the consequence of the increasing thermal parameter Θ through decreasing T_0 (Eq. (3) and Fig. 4). Low Γ values such as $\Gamma = 1$ do not permit to explain η values higher than ~ 1.3 . Large Γ ($\Gamma = 8$) seems to be required to explain the highest measured η values, especially the three points with $\eta = 1.5$ –1.8 at 13–18 AU and a few points with $\eta \sim 2.0$ –2.5 at 35–50 AU. However, as can be seen for the density distribution of red points in Fig. 11, this case underpredicts the number of low η (< 1.3) values at $r_h > 25$ AU. Overall, $\Gamma = 2.5$ provides the best fit.

Continuing with the assumption of a unique Γ value, we studied the sensitivity of the results to the assumed distribution of the β values. Specifically, we considered two extreme cases: (i) a uniform distribution of $|\beta|$ values between 0° and $+90^\circ$, which occurs in a situation where all spin axes are in the ecliptic plane but objects are seen at a random “season”; and (ii) a single $\beta = 0^\circ$ value, i.e. all spin axes are perpendicular to the line-of-sight (i.e., ecliptic plane). Results are shown in Fig. 12. The uniform β models (top panels) also permit a satisfactory interpretation of the measurements. Actually, with a minimum distance $d = 0.09$ and a p_{KS} value of 0.64 for

the random roughness case, the fit is even better than with the previous nominal model (uniform spin axis distribution on the sphere). In this case, the best fit Γ values are typically twice higher than in the nominal model. The top right panel of Fig. 12 shows Monte-Carlo simulations for this β distribution and $\Gamma = (2, 5$ and 15) MKS. Comparing the $\Gamma = 5$ MKS model with the previous $\Gamma = 2.5$ MKS case of Fig. 11, the slight improvement in the fit can be seen in that the new case permits to account for more points with high η without underpredicting the number of points with low η (an effect of the increased number of high β values in the uniform distribution). In contrast, the $\beta = 0^\circ$ models (bottom panels of Fig. 12) can be excluded. In the random roughness case, the minimum K-S distance never drops below 0.25 ($p_{KS} \sim 4 \times 10^{-4}$), the problem being that the single β value leads to too narrow a distribution of the η values for a given r_h , as can be seen in the bottom right panel of Fig. 12. The situation is of course even worse for the other three roughness (“fixed”) cases ($p_{KS} \sim 10^{-5}$ at best) since in this case the η distribution for fixed r_h is infinitely narrow (following Fig. 5). We conclude that our data can exclude the situation where all spin axes are perpendicular to the line-of-sight, i.e.

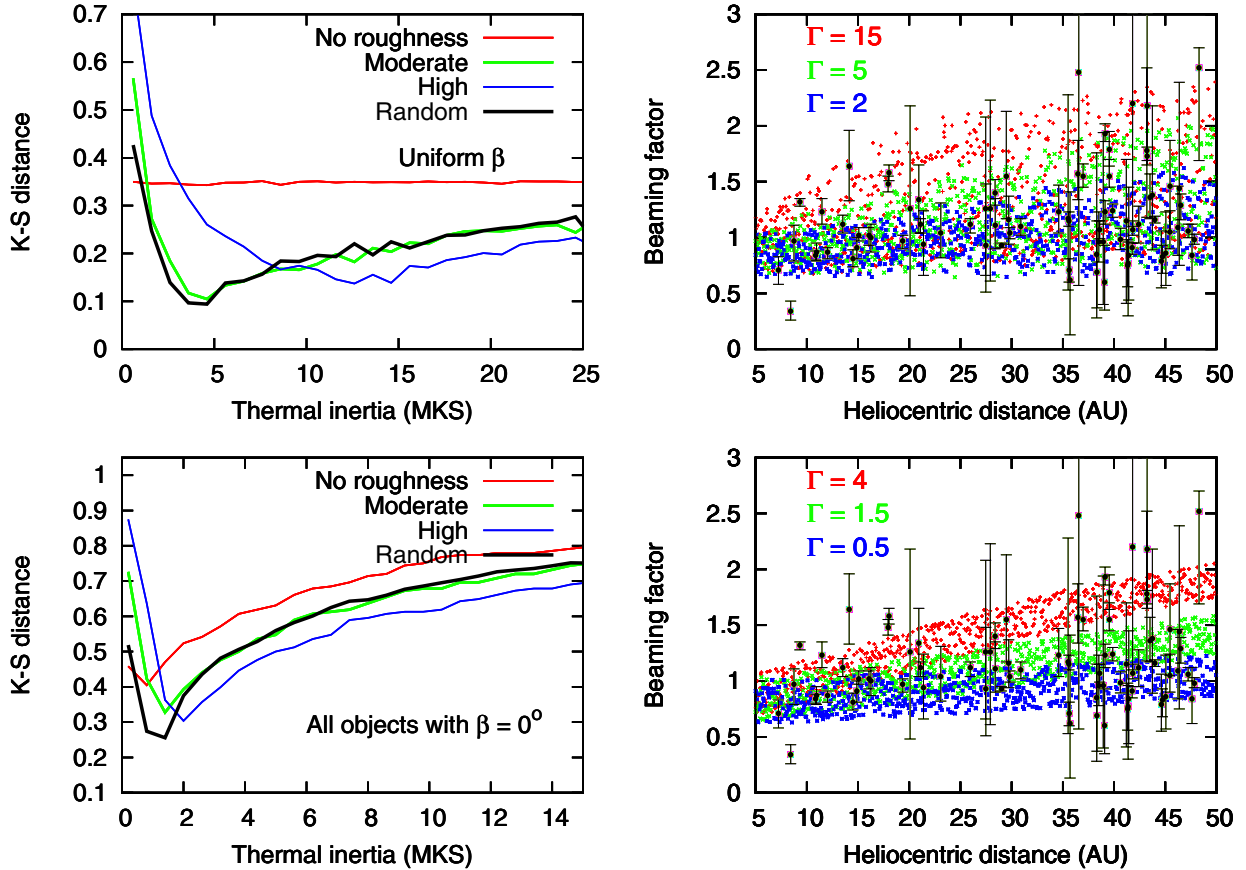


Fig. 12. *Left:* Kolmogorov-Smirnov distance d and Monte-Carlo simulations for the two assumed alternative distributions of polar axes. *Top:* uniform distribution of β s between $\pm 90^\circ$ (i.e. spin axes in ecliptic plane). *Bottom:* all objects with $\beta = 0^\circ$ (i.e. spin axes perpendicular ecliptic plane). In each case, the K-S distance to the data is plotted (*left panels*) as a function of Γ for the four roughness cases. *Right panels* show Monte-Carlo simulations for the random roughness cases.

all objects are seen equator-on. Regarding the other orientation distributions, although the scenario favoring higher obliquities (all spin axes in the ecliptic plane) permits improved fits compared to the uniform orientation on a sphere, we cannot formally reject the latter. While some planetesimal formation scenarios suggest the spins may have originally been aligned perpendicularly to the ecliptic (Johansen & Lacerda 2010) there are possible evolutionary pathways to high obliquity spins (Lacerda 2011).

Coming back to the uniform orientation of the polar axes on the sphere and random roughness cases, and to follow-up on the results suggested in Sect. 4.1, we investigated cases in which the thermal inertia was allowed to vary with heliocentric distance. Specifically, the KS test was done separately on three bins in heliocentric distance, namely $r_h < 25$ AU, $25 < r_h < 41$ AU, and $r_h > 41$ AU. The first bin corresponds to the region of Centaurs and closest SDOs, and the other two split the remaining TNOs in two groups of approximately equal size (most objects in the last bin have $r_h < 53$ AU). Results, shown in Fig. 13 (left panel), indicate that the minimum KS distance between observations and models is achieved for higher values of the thermal inertia at lower heliocentric distances. The same behavior is shown by the histograms of best fit solutions Γ_0 when measurement errors are considered (right panel). These histograms indicate mean values for Γ_0 of 5 ± 1 MKS at $r_h < 25$ AU, 2.5 ± 0.5 MKS at $25 < r_h < 41$ AU, and 2 ± 0.5 MKS at $r_h > 41$ AU. Although the error bars for the nearest two distance bins overlap, the histograms are strongly suggestive of an actual decrease of the thermal inertia with increasing heliocentric distance, consistent with inferences from Sect. 4.1.

Finally we briefly studied the dependence of Γ on geometric albedo. For this the Monte-Carlo calculations and the Kolmogorov-Smirnov test were performed in the (p_V, η) space. A difference with all previous simulations is that this time, synthetic objects had the same r_h and p_V as the real ones. Fixing the r_h to the observational values was needed because the $\eta(\Gamma)$ relationship is so strongly r_h -dependent. Thus, for each of the 85 observed objects we created 100 clones that differed only in their β value, chosen randomly from a uniform distribution on the sphere. As before, a rotation period of 8 h and the random roughness case were used. Figure 14 compares results for the previous solution having $\Gamma = 2.5$ MKS for all objects (see Fig. 11) with a simulation in which all objects having geometric albedos higher than 20% are assigned a much lower thermal inertia, $\Gamma = 0.5$ MKS. The visual improvement brought by the latter case is supported by the K-S distance, which in (p_V, η) space, decreases from 0.17 for constant Γ to 0.12 for p_V -dependent Γ . A qualitatively similar result is achieved in tests in which the thermal inertia is imposed to drop at large diameters, e.g. $\Gamma = 1$ at $D > 700$ km. Thus, the trend of a decreasing thermal inertia already suggested from the fixed orientation cases (Fig. 7) is confirmed by this analysis. Note that the drop in Γ required from the bright objects – from 2.5 to 0.5 MKS – is much more drastic than the general decrease of Γ with heliocentric distance. Thus, in spite of the correlation between p_V and r_h in our sample, this indicates a specific behavior of the high-albedo objects. Makemake ($p_V = 0.77 \pm 0.02$, $\eta = 2.29^{+0.46}_{-0.40}$) appears to be an exception to the picture, as it cannot be fit with $\Gamma = 0.5$ MKS.

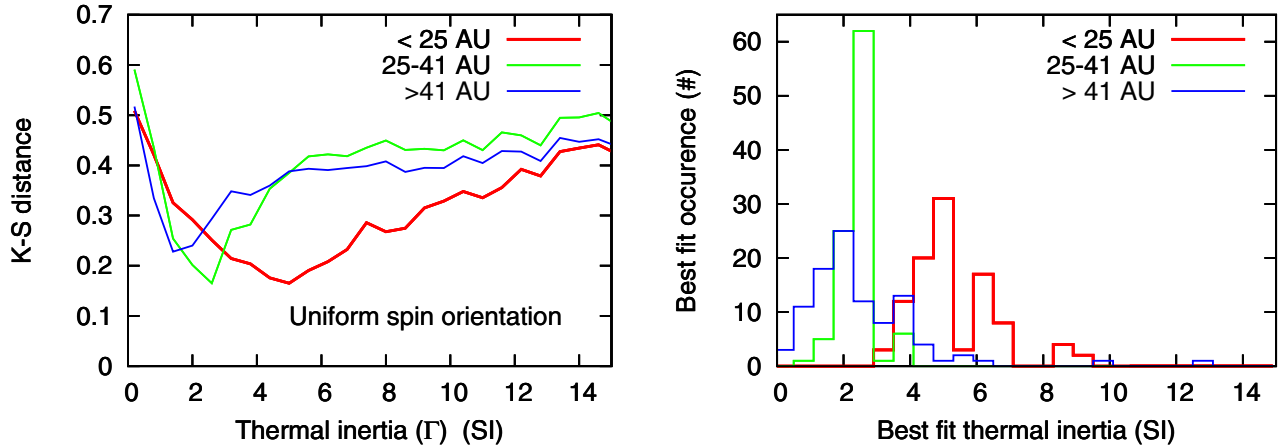


Fig. 13. *Left:* Kolmogorov-Smirnov distance d between observed and modeled distribution of η grouping data by bins of heliocentric distance ($r_h < 25$ AU, $25 < r_h < 41$ AU, and $r_h > 41$ AU). In all models, a uniform distribution of the polar axes over the sphere and the “random roughness” case are assumed. *Right:* histograms showing the distribution of best fit Γ_0 , when accounting for uncertainties in the measured η .

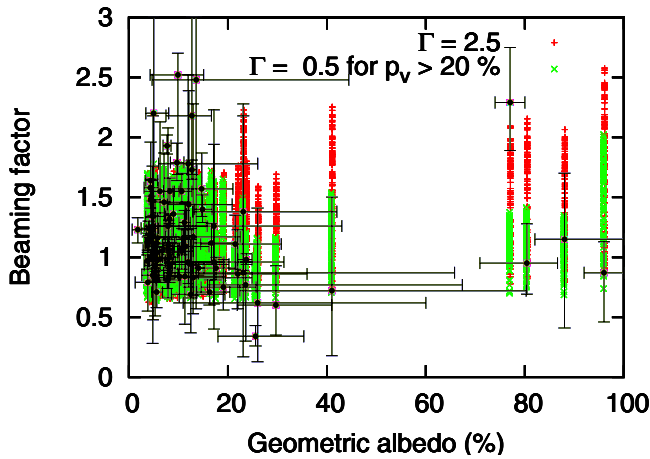


Fig. 14. Beaming factor η as a function of geometric albedo p_V for the entire sample, compared with Monte-Carlo simulations assuming a rotation period of 8 h, a random orientation of the polar axes, uniform on the sphere, and a random distribution of surface roughnesses. The synthetic objects have the same r_h values as in the observations. Cases with (i) a constant thermal inertia $\Gamma = 2.5$ MKS (red points) and (ii) $\Gamma = 2.5$ MKS for objects with $p_V < 20\%$ and $\Gamma = 0.5$ MKS for objects with $p_V > 20\%$ (green points) are shown. The latter case allows an improved match of the observations, except for Makemake ($p_V = 0.77 \pm 0.02$, $\eta = 2.29^{+0.46}_{-0.40}$).

5. Discussion

We have used two different approaches to determine the thermal inertia of TNO/Centaurs using their measured beaming factors. The first method consists of considering cases with fixed object orientation and roughness, – four orientations/roughness combinations have been included. The second method is a Monte-Carlo simulation of the population with a random distribution of orientations and surface roughnesses, in which the calculated beaming factors are compared to the observed values by means of the Kolmogorov-Smirnov test. Both approaches converge to suggest that TNO/Centaurs have low thermal inertia. The first method indicates a median value of Γ in the range 1.7–4.2 MKS, while the second yields a best-fit value $\Gamma = 2.5$ MKS for the most likely case where spin axes have a uniform distribution of orientation over the sphere (and only twice greater if all spin

Table 6. Thermal inertias: comparison with previous work.

Object	Γ (MKS) this work	Γ (MKS) previous work	Ref.
Chiron	1.5–5	<3 (smooth); 5–10 (rough)	(1)
Chariklo	5–14	3–30 (10–20 preferred)	(1)
Quaoar	3.5–22	2–10*	(1)
Orcus	0.4–1.2	0.4–2.0	(1)
2003 AZ ₈₄	0.6–1.8	2–10*	(2)
Haumea	0.2–0.5	0.1–1	(3)
Phoebe	15–45	20–25	(4)

References. (1) Fornasier et al. (2013); (2) Müller et al. (2010); (3) Santos-Sanz et al. (2010); (4) Howett et al. (2010).

Notes. (*) See text for discussions.

axes are in the equatorial plane). In addition, the two methods qualitatively agree on a decrease of thermal inertia with heliocentric distance. The “fixed orientation/roughness” model indicates a steep variation, with power exponent of about -1.7 . The statistical approach points to a more gentle decrease of Γ , by a nominal factor of 2.5 from 8–25 to 41–53 AU, which is roughly equivalent to a power exponent of ~ -1 .

5.1. Comparison with results from thermophysical models

For a limited number of objects of the combined *Spitzer/Herschel* sample, more detailed thermophysical modeling (TPM) has been performed to determine thermal inertia and the sensitivity of the results to pole orientation, rotation period and surface roughness. Such models have been presented especially by Müller et al. (2010) and Lim et al. (2010) using an early version of the *Herschel* fluxes, and more extensively by Fornasier et al. (2013). In the case of Haumea, an estimate of its thermal inertia was obtained by Santos-Sanz et al. (2010) from preliminary TPM of its thermal lightcurve (Lellouch et al. 2010). Results from six prominent objects are gathered in Table 6 and compared to values from our work. For the latter, the indicated range encompasses the four (orientation, roughness) cases but does not account for the measurement error bars (note also that although for most of them, the rotational period is known, the

results quoted here are those obtained from $P = 8$ h). The overall agreement between this and previous work is heartening and lends support to our simpler method. The higher value of Γ found on 2003 AZ₈₄ by Müller et al. (2010) results from their higher η (1.31 ± 0.08), based on preliminary observations and reductions. For Quaoar, Fornasier et al. (2013) quote a thermal inertia in the 2–10 MKS range, but as can be seen for their Fig. 13, fitting solutions (reduced $\chi^2 < 1$) include thermal inertias up to 25 MKS, in agreement with the 4–25 MKS range estimated in this work.

5.2. Thermal inertia and dependence with heliocentric distance

We now turn to comparing our population results to expectations based on the properties of ices. The thermal inertia is expressed as $\Gamma = \sqrt{\kappa\rho c}$, where κ is the thermal conductivity, ρ is surface density, and c in the specific heat. All of these quantities vary with surface composition and temperature, but we here consider H₂O-ice surfaces, which are by far the most common in the Kuiper belt (e.g. de Bergh et al. 2013), and assume a constant $\rho = 1000$ kg m⁻³. The temperature dependence of c and κ has been studied by a number of authors, and a recent compilation has been presented by Castillo-Rogez et al. (2012). For crystalline ice – which is the form of ice found on virtually all of the H₂O-ice objects – expressions given in Table C1 of that paper lead to an almost constant thermal inertia over 150–30 K, increasing from 2100 to 2600 MKS. For amorphous ice, literature indicates conflicting results (by ~4 orders of magnitude!) on the thermal conductivity. Using the expression given by Klinger (1980) for κ in combination with that quoted for c by Castillo-Rogez et al. (2012) leads to a variation of the thermal inertia from 715 to 160 MKS over 150–30 K (i.e. a quasi-linear variation). Using instead the (assumed temperature-independent) value of κ reported by Kouchi et al. (1992) ($\kappa = 10^{-4}$ W m⁻¹ K⁻¹) would instead give $\Gamma = 12$ –5 MKS over 150–30 K, but according to Ross & Kargel (1998), the Kouchi et al. (1992) measurements have been refuted by Andersson & Suga (1994). Thus, dismissing this latter case, the Γ value for compact H₂O ice is typically two (for amorphous ice) to three (crystalline) orders of magnitude higher than we determine on TNO surfaces, and their expected variation with temperature is at most proportional to T (i.e. to $r_h^{-1/2}$) for amorphous ice and nearly T - (i.e., r_h -) independent for the more likely case of crystalline ice.

Surface porosity and granularity strongly reduce the thermal conductivity, and are likely to be the cause of the measured low thermal inertias (e.g. Espinasse et al. 1991; Shoshany et al. 2002; Guilbert-Lepoutre et al. 2011). Based on a fractal porous model of cometary ice, Shoshany et al. (2002) propose an analytic expression for the effective thermal conductivity as a function of porosity p (defined as the fraction of the volume occupied by voids), in the form of a temperature-independent correction factor $\Phi = (1 - p/p_c)^{4.1p+0.22}$, where $p_c = 0.7$ the porosity at percolation threshold. This expression yields a steep decrease of Γ when p approaches p_c , i.e. $\Phi = 0.01$ –0.001 for $p = 0.58$ –0.64. This model (which reduces the surface density by only a factor of 2–3) therefore easily accounts for thermal inertias much lower than that of compact ices, without changing its temperature dependence.

However, the above expression ignores the effect of pore conductivity, which may become dominant near the limiting porosity p_c . Within empty pores, heat is transferred through thermal radiation, inducing an effective conductivity $k_{\text{pore}} = 4r_{\text{pore}}\epsilon\sigma T^3$. In the most frequent case of crystalline ice, pore

sizes of 25 μm (for $T = 150$ K) – 3000 μm (for $T = 30$ K) are required to produce a thermal inertia of 2.5 MKS. Comparing with the (vastly uncertain) particle sizes invoked from modeling near-IR spectra, these numbers suggest that the radiative contribution to conductivity may be important, especially for the high temperature case. In this regime, κ scales as T^3 , and combined with the temperature-dependence of the specific heat (see Castillo-Rogez et al. 2012) yields a Γ approximately proportional to $T^{1.8}$ for crystalline ice and to T^2 for amorphous ice. Therefore, if the heat transfer is dominated by radiative effects between particles, a r_h^{-1} dependence for Γ is expected. This behavior is consistent with a factor-of-2.5 decrease of the thermal inertia from the Centaur (8–25 AU) region to the outer part of the Kuiper belt at 41–53 AU. It would still not be sufficient to explain a steeper $\sim r_h^{-1.7}$ variation, as suggested from the “fixed orientation/roughness” approach.

5.3. Comparison with other distant icy bodies and dependence with rotation period and albedo

While thermal inertia has been measured for a relatively large number of main-belt and near-Earth asteroids, revealing a convincing trend of a decrease with size (Delbo’ et al. 2007), measurements on icy bodies are more scarce. Spatially-resolved, spacecraft-borne observations of diurnal curves have provided values for Jupiter Galilean satellites and most of Saturn’s satellites (see Howett et al. 2010 and references therein). Inferred values, that refer to a skin depth associated with the diurnal timescale, are typically 50–70 MKS for Jupiter’s satellites and 5–20 MKS for Saturn’s (except in some specific regions of Mimas and Tethys, likely affected by electronic bombardment from Saturn’s magnetosphere, see Howett et al. 2011, 2012). This difference is probably indicative of a higher degree of compaction (enhanced density, reduced porosity) on the surface of Jupiter’s vs. Saturn’s icy moons. At greater distance from the Sun, the thermal inertia on Uranus moons is rather unconstrained, as their surface temperature, measured from the shape of the H₂O ice bands in the near-IR (Grundy et al. 1999), is not determined with sufficient accuracy. No results are available for Neptune’s satellites (except for not directly comparable constraints on the seasonal thermal inertia of Triton’s surface based on seasonal pressure/polar cap models, e.g. Hansen & Paige 1992). In contrast, the thermal inertia of Pluto’s and Charon’s surfaces has been determined from the system thermal lightcurve, and found to be 25 ± 5 MKS for Pluto (relevant to the CH₄/tholin areas), and most probably in the range 10–20 MKS for Charon (Lellouch et al. 2011).

The thermal inertia values determined in this study are, at comparable distances, lower than both on the Saturn’s H₂O-covered satellites and in the Pluto-Charon system. We put aside the case of Pluto, whose surface texture may be affected by the seasonal condensation/sublimation cycles of N₂ and CH₄, and where thermal inertia may also be enhanced by gas conduction within surface pores (Lellouch et al. 2000). Nonetheless we argue that the lower thermal inertia on the “average TNO” does not necessarily indicate different surface properties compared to either Charon or Saturn’s moons. The skin depth, i.e. the depth into the surface probed by the thermal measurements, can be expressed as $d_s = \frac{\Gamma}{\rho c \sqrt{\omega}} = \sqrt{\frac{k}{\rho c \omega}}$. The mean rotation period of TNOs is 8 h, vs. 1–5 days for most of the Saturn’s satellites (except Phoebe and Iapetus) and 6.4 days for Charon. Hence, for equal density/thermal properties, the diurnal wave probes shallower levels in the surface on fast rotating TNOs. The order of

magnitude of the thermal skin depth is 1 cm (e.g. 0.1 cm for the “average TNO” and 2 cm for Charon, using the measured Γ). Hence, at least qualitatively, a thermal inertia increasing with depth over the first cm into the surface would account for the observed behavior. Such a behavior is actually observed on the regolith of the Moon (Keihm 1984) and Mercury (Mitchell & de Pater 1994), and has also been shown to occur on asteroid 21 Lutetia (Gulkis et al. 2012), with an increase of Γ from about 5 MKS to 30 MKS over a 5 cm depth. Another example of this situation is the fact that the thermal inertia of Galilean satellites as determined from eclipse measurements, i.e. on a ~ 3 h timescale, is only 10–15 MKS, vs. 50–70 MKS inferred from diurnal curves (see Howett et al. 2010). Validating this scenario for TNOs will require implementing models including a specific vertical profile of thermal conductivity and density into the surface, coupled with a description of the absorbing properties of the subsurface. For now, we caution on incorrect conclusions that might be reached from oversimplified reasoning. For example, two objects with the same rotation period but different measured values of thermal inertia must have different surface/subsurface properties. Yet, based on a simple argument invoking different d_s (proportional to Γ) one might be tempted to conclude that the two objects have the same surface/subsurfaces, but probed at different levels.

Finally we find that objects with high albedos ($>20\%$) tend to have lower beaming factors than the bulk of the population (Fig. 2), indicative of a lower thermal inertia (typically 0.5 MKS, see Figs. 7 and 14). A plausible explanation is that in addition to a specific composition (e.g. pure ice), a high albedo reflects a strongly scattering surface characterized by small grains. In a porous surface, the size of the pores is comparable to the size of the grains. Thus, in a regime where radiative conductivity is important and proportional to pore radius, one may expect that the thermal conductivity drops for high albedo objects. We note that given the positive correlation between diameter and geometric albedo in our sample, these low thermal inertias may also be viewed as being a characteristic of the large-sized objects (>700 km). The two aspects are probably related as large objects may be able to retain small grain regolith on their surfaces. This explanation is put forward by Delbo’ et al. (2007) to account for the trend of decreasing thermal inertia with increasing diameter in the asteroid belt. With a geometric albedo of 0.77 and a beaming factor of ~ 2.3 , Makemake appears to be an outlier in this picture. In the “fixed orientation/roughness model” this η value indicates a thermal inertia of at least 5–7 MKS (obtained with $\beta = 0^\circ$), and the Monte-Carlo simulations (Fig. 14) indicate that $\Gamma = 0.5$ MKS clearly provided a worse fit to this object than the mean 2.5 MKS value. The cause for this behavior is intriguing. Makemake is in the regime of volatile retention (Schaller & Brown 2007), and its 52 AU distance and the apparent presence of a dark and warm (~ 50 K) surface unit (Lim et al. 2010) make it an a priori plausible candidate for currently holding a CH_4 or N_2 atmosphere. Thus it might be tempting to attribute the anomalous thermal inertia to atmospheric conduction within surface pores. Based on Mendis & Brin (1977) equations for atmospheric-assisted thermal conductivity (proportional to atmospheric pressure), Lellouch et al. (2000) estimated that this process may contribute to the thermal inertia of Pluto, where the pressure is ~ 20 μbar . In the case of Makemake, however, stellar occultation observations provide an upper limit to any global atmosphere at the level of 4–12 nbar (Ortiz et al. 2012). This probably rules out the explanation, especially because the measured thermal inertia refers to Makemake’s bright terrains, where an atmosphere is not likely to exist. More detailed, multi-terrain,

thermophysical models (as preliminary presented by Müller et al. 2011) are deferred to a future study.

6. Summary

In the framework of a NEATM model, *Herschel/Spitzer* thermal observations provide diameter, albedo and beaming factors for TNOs/Centaurs. We have used a set of published, updated or new values for 85 objects to characterize in a statistical sense the thermal properties of the population. For this, a thermophysical model including surface roughness and different assumptions on the objects rotation state was developed. We used (i) “fixed spin/roughness” models, in which all objects are assumed to have the same surface roughness, spin orientation and period and (ii) a Monte-Carlo approach whereby synthetic datasets of beaming factors are created from random distributions of spin orientation and surface roughness. The main conclusions can be summarized as follows:

- Beaming factors η range from values <1 to ~ 2.5 , but high η values are lacking at low heliocentric distances (e.g. there are no objects with $\eta > 2$ at $r_h < 30$ AU). Beaming factors <1 are frequent and indicate that surface roughness effects are important.
- The mean thermal inertia in the population is found to be $\Gamma = (2.5 \pm 0.5) \text{ J m}^{-2} \text{ s}^{-1/2} \text{ K}^{-1}$
- There is a strong suggestion that the thermal inertia decreases with heliocentric distance, from Γ_0 of $(5 \pm 1) \text{ J m}^{-2} \text{ s}^{-1/2} \text{ K}^{-1}$ at $r_h < 25$ AU to $(2.5 \pm 0.5) \text{ J m}^{-2} \text{ s}^{-1/2} \text{ K}^{-1}$ at $25 < r_h < 41$ AU, and $(2 \pm 0.5) \text{ J m}^{-2} \text{ s}^{-1/2} \text{ K}^{-1}$ at $r_h = 41\text{--}53$ AU.
- These thermal inertias are 2–3 orders of magnitude lower than expected for compact ices and, for comparable distances, are generally lower than on Saturn’s satellites or in the Pluto/Charon system.
- Objects with high albedos ($>20\%$) have lower beaming factors than the rest of the population, i.e. unusually low thermal inertias. This possibly results from smaller grain size. An exception is Makemake.
- While the measured thermal inertia cannot be directly associated to a specific surface composition, the ensemble of our results suggests strongly porous surfaces, in which the heat transfer is affected by radiative conductivity within pores and increases with depth in the subsurface.

Acknowledgements. We acknowledge financial support by the French Program National de Planétologie and Centre National de la Recherche Scientifique (CNRS). M. Mommert acknowledges support through the DFG Special Priority Program 1385. E. Vilenius was supported by the German *DLR* project number 50 OR 1108. P. Santos-Sanz acknowledges financial support by Spanish grant AYA2008-06202-C03-01. The work of Cs. Kiss has been supported by the PECS-98073 grant of the European Space Agency and the Hungarian Space Office, the K-104607 grant of the Hungarian Research Fund (OTKA) and the Bolyai Research Fellowship of the Hungarian Academy of Sciences.

References

- Allen, D. A. 1970. *Nature*, 227, 158
 Alvarez-Candal, A., Delsanti, A., et al. 2009, *AJ*, 137, 315
 Andersson, O., & Suga, H. 1994, *Phys. Rev. B*, 50, 6583
 Bauer, J. M., Buratti, B. J., Simonelli, D. P., & Owen, W. M., Jr. 2004, *ApJ*, 610, L57
 Bauer, J. M., Grav, T., Buratti, B. J., & Hicks, M. D. 2006, *Icarus*, 184, 181
 Benecchi, S. D., Noll, K. S., Grundy, W. M., et al. 2009, *Icarus*, 200, 292
 Brown, M. E., & Schaller, E. L. 2007, *Science*, 316, 1585
 Brown, M. E., & Trujillo, C. A. 2004, *AJ*, 127, 2413
 Brown, M. E., Trujillo, C. A., & Rabinowitz, D. L. 2005, *ApJ*, 635, L97
 Brown, M. E., Schaller, E. L., Roe, H. G., Rabinowitz, D. L., & Trujillo, C. A. 2006, *ApJ*, 643, L61

- Brown, M. E., Burgasser, A. J., & Fraser, W. C. 2011, *ApJ*, 738, L26
- Brucker, M. J., Grundy, W. M., Stansberry, J. A., et al. 2009, *Icarus*, 201, 284
- Buratti, B., Soderlund, B., Bauer, J., et al. 2008, *Icarus*, 193, 309
- Bus, S. J., Bowell, E., Harris, A. W., & Hewitt, A. V. 1989, *Icarus*, 77, 223
- Castillo-Rogez, J. C., Johnson, T. V. Thomas, P. C., et al. 2012, *Icarus*, 219, 86
- Chandrasekhar, S. 1987, *Ellipsoidal figures of equilibrium* (New York: Dover)
- Cruikshank, D. P., Stansberry, J. A., Emery, J. P., et al. 2005, *ApJ*, 624, L53
- Davidsson, B. J. R., Gutierrez, P. J., Rickman, H. 2009, *Icarus*, 201, 335
- Davies, J. K., McBride, N., Ellison, S. L., Green, S. F., & Ballantyne, D. R. 1998, *Icarus*, 134, 213
- de Bergh, C., Schaller, E. L., Brown, M. E., et al. 2013, in *The science of Solar System Ices ASSL*, 356, 107
- Delbo', M., dell'Oro, A., Harris, A. W., Mottola, S., & Mueller, M. 2007, *Icarus*, 190, 236
- Dotto, E., Perna, D., Barucci, M. A., et al. 2008, *A&A*, 490, 829
- Duffard, R., Ortiz, J. L., Santos Sanz, P., et al. 2008, *A&A*, 479, 877
- Duffard, R., Ortiz, J. L., Thirouin, A., et al. 2009, *A&A*, 505, 1283
- Duffard, R., Pinilla-Alonso, N., Santos-Sanz, P., et al. 2013, *A&A*, submitted
- Elliot, J. L., Kern, S. D., Clancy, K. B., et al. 2005, *AJ*, 129, 1117
- Elliot, J. L., Person, M. J., Zuluaga, C. A., et al. 2010, *Nature*, 465, 897
- Emery, J. P., Sprague, A. L., Witteborn, F. C., et al. 1998, *Icarus*, 136, 104
- Engelbracht, C. W., Blaylock, M., Su, K. Y. L., et al. 2007, *PASP*, 119, 994
- Espinasse, S., Klinger, J., Ritz, C., & Schmitt, B. 1991, *Icarus*, 92, 350
- Farnham, T. L. 2001, *Icarus*, 152, 238
- Fornasier, S., Lellouch, E., Müller, T., et al. 2013, *A&A*, 555, A15
- Gaudi, B. S., Stanek, K. Z., Hartman, J. D., Holman, M. J., & McLeod, B. A. 2005, *ApJ*, 629, L49
- Gordon, K. D., Engelbracht, C. W., Fadda, D., et al. 2007, *PASP*, 119, 1019
- Grav, T., Mainzer, A. K., Bauer, J., et al. 2011, *ApJ*, 742, 40
- Griffin, M. J., Abergel, A., Abreu, A., et al. 2001 *A&A*, 518, L3
- Grundy, W. M., Buie, M. W., Stansberry, J. A., Spencer, J. R., & Schmitt, B. 1999, *Icarus*, 142, 536
- Grundy, W. M., Noll, K. S., & Stephens, D. C. 2005, *Icarus*, 176, 184
- Grundy, W. M., Stansberry, J. A., Noll, K. S., et al. 2007, *Icarus*, 191, 286
- Grundy, W. M., Noll, K. S., Virtanen, J., et al. 2008, *Icarus*, 197, 260
- Grundy, W. M., Noll, K. S., Nimmo, F., et al. 2011, *Icarus*, 213, 678
- Guilbert-Lepoutre, A., Lasue, J., Federico, C., et al. 2011, *A&A*, 529, A71
- Gulkis, S., Keihm, S., Kamp, L., et al. 2012, *Planet. Space Sci.*, 66, 31
- Hansen, C., & Paige, D. A. 1992, *Icarus*, 99, 273
- Hapke, B. W. 1984, *Icarus*, 59, 41
- Harris, A. W. 1998, *Icarus*, 131, 291
- Harris, A. W. 2006, *Proc. IAU Symp.* 229 (Cambridge, UK: Cambridge Univ. Press), 449
- Hoffmann, M., Fink, U., Grundy, W. M., & Hicks, M. 1992, *Liège International Astrophysical Colloquia* (Liège: Université de Liège), 30, 203
- Howett, C. J. A., Spencer, J. R., Pearl, J., et al. 2010, *Icarus*, 206, 573
- Howett, C. J. A., Spencer, J. R., Schenk, P., et al. 2011, *Icarus*, 216, 221
- Howett, C. J. A., Spencer, J. R., Hurford, T., Verbiscer, A., & Segura, M. 2012, *Icarus*, 221, 1084
- Jewitt, D. C. 2009, *AJ*, 137, 4296
- Johansen, A., & Lacerda, P. 2010, *MNRAS*, 404, 475
- Keihm, S. J. 1984, *Icarus*, 60, 568
- Kern, S. D., McCarthy, D. W., Buie, M. W., et al. 2000, *ApJ*, 542, L155
- Kiss, Cs., Szabó, Gy., Horner, J., et al. 2013a, *A&A*, 555, A3
- Kiss, Cs., Müller, T., Vilenius, E., et al. 2013b, *Exp. Astron.*, submitted
- Klinger, J., 1980, *Science*, 209, 271
- Kouchi, A., Greenberg, J. M., Yamamoto, T., & Mukai, T. 1992, *ApJ*, 388, L73
- Lacerda, P. 2011, *AJ*, 142, 90
- Lacerda, P., & Luu, J. 2003, *Icarus*, 161, 174
- Lacerda, P., & Luu, J. 2006, *AJ*, 131, 2314
- Lacerda, P., & Jewitt, D. C. 2007, *AJ*, 133, 1393
- Lagerros, J. S. V. 1996, *A&A*, 310, 1011
- Lagerros, J. S. V. 1998, *A&A*, 332, 1123
- Lebofsky, L. A., & Spencer, J. R. 1989, in *Asteroids II*, 128
- Lellouch, E., Laureijs, R., Schmitt, B., et al. 2000, *Icarus*, 147, 220
- Lellouch, E., Kiss, C., Santos-Sanz, P., et al. 2010, *A&A*, 518, L147
- Lellouch, E., Stansberry, J., Emery, J., Grundy, W., & Cruikshank, D. P. 2011, *Icarus*, 214, 701
- Lim, T. L., Stansberry, J., Müller, T. G., et al. 2010, *A&A*, 518, L148
- Mainzer, A., Grav, T., Masiero, J., et al. 2011a, *ApJ*, 743, 156
- Mainzer, A., Grav, T., Masiero, J., et al. 2011b, *ApJ*, 736, 100
- Maris, M., Carraro, G., & Parisi, M. G. 2007, *A&A*, 472, 311
- Masiero, J. R., Mainzer, A. K., Grav, T., et al. 2011, *ApJ*, 741, 68
- Mendis, D. A., & Brin, G. D. 1977, *The Moon*, 17, 359
- Miller, C., Verbiscer, A. J., Chanover, N. J., Holtzman, J. A., & Helfenstein, P. 2011, *Icarus*, 212, 819
- Mitchell, D. L., & de Pater, I. 1994, *Icarus*, 110, 2
- Mommert, M., Harris, A. W., Kiss, Cs., et al. 2012, *A&A*, 541, A93
- Mueller, M., Delbo', M., Hora, J. L., et al. 2011, *AJ*, 141, 109
- Müller, T. G., Lellouch, E., Bönhardt, H., et al. 2009, *Earth Moon Planets*, 105, 209
- Müller, T. G., Lellouch, E., Stansberry, J., et al. 2010, *A&A*, 518, L146
- Müller, T. G., Lellouch, E., Kiss, C., et al. 2011, *EPSC-DPS Joint Meeting*, 1416
- Ortiz, J. L., Gutiérrez, P. J., Casanova, V., & Sota, A. 2003, *A&A*, 407, 1149
- Ortiz, J. L., Gutiérrez, P. J., Santos-Sanz, P., Casanova, V., & Sota, A. 2006, *A&A*, 447, 1131
- Ortiz, J. L., Morales, N., Duffard, R., et al. 2010, *IAU Circ.*, 9184, 1
- Ortiz, J.-L., Sicardy, B., Braga-Ribas, F., et al. 2012, *Nature*, 491, 566
- Osip, D. J., Kern, S. D., & Elliot, J. L. 2003, *Earth Moon Planets*, 92, 409
- Pál, A., Kiss, Cs., Müller, T. G., et al. 2012, *A&A*, 541, A6
- Perna, D., Barucci, M. A., Fornasier, S., et al. 2010, *A&A*, 510, A53
- Pilbratt, G. L., Riedinger, J. R., Passvogel, T., et al. 2010, *A&A*, 518, L1
- Proglitsch, A., Waelkens, C., Geis, N., et al. 2010, *A&A*, 518, L2
- Press, A., Teukchsky, S. A., Vetterling, W. T., & Flannery, B. P. 1992, *Numerical Recipes* (Cambridge: University Press)
- Rabinowitz, D. L., Barkume, K., Brown, M. E., et al. 2006, *ApJ*, 629, 1238
- Rabinowitz, D. L., Schaefer, B. E., & Tourtellotte, S. W. 2007, *AJ*, 133, 26
- Rieke, G. H., Young, E. T., Engelbracht, C. W., et al. 2004, *ApJS*, 154, 25
- Roe, H. G., Pike, R. E., & Brown, M. E. 2008, *Icarus*, 198, 459
- Romanishin, W., & Tegler, S. C. 1999, *Nature*, 398, 129
- Romon, J., de Bergh, C., Barucci, M. A., et al. 2001, *A&A*, 376, 310
- Ross, R. G., & Kargel, J. S. 1998, in *Solar System Ices* (Kluwer Academic), ASSL, 227, 33
- Rousselot, P., Petit, J.-M., Poulet, F., & Sergeev, A. 2005a, *Icarus*, 176, 478
- Rousselot, P., Levasseur-Regourd, A. C., Muinonen, K., & Petit, J.-M. 2005b, *Earth Moon Planets*, 97, 353
- Rozitis, B., & Green, S. F. 2011, *MNRAS*, 415, 2042
- Russell, H. N. 1916, *ApJ*, 43, 173
- Santos-Sanz, P., Lellouch, E., Fornasier, S., et al. 2010, *BAAS*, 42, 1013
- Santos-Sanz, P., Lellouch, E., Fornasier, S., et al. 2012, *A&A*, 541, A92
- Schaller, E. L., & Brown, M. E. 2007, *ApJ*, 659, L61
- Sheppard, S. S. 2007, *AJ*, 134, 787
- Sheppard, S. S. 2010, *AJ*, 139, 1394
- Sheppard, S. S., & Jewitt, D. C. 2002, *AJ*, 124, 1757
- Sheppard, S. S., & Jewitt, D. C. 2003, *Earth Moon Planets*, 92, 207
- Shoshany, Y., Prialnik, D., & Podolak, M. 2002, *Icarus*, 157, 219
- Sicardy, B., Ortiz, J. L., Assafin, M., et al. 2011, *Nature*, 478, 493
- Spearman, C. 1904, *Am. J. Psychol.*, 57, 72
- Spencer, J. R. 1990, *Icarus*, 83, 27
- Spencer, J. R., Lebofsky, A. L., & Sykes, M. V. 1989, *Icarus*, 78, 337
- Stansberry, J. A., Grundy, W. M., Margot, J. L., et al. 2006, *ApJ*, 643, 556
- Stansberry, J. A., Gordon, K. D., Bhattacharya, B., et al. 2007, *PASP*, 119, 1038
- Stansberry, J., Grundy, W., Brown, M., et al. 2008, in *The Solar System Beyond Neptune*, eds. M. A. Barucci, et al. (Tucson: Univ. of Arizona Press), 161
- Tedesco, E. F., Noah, P. V., Noah, M., & Price, S. D. 2002, *AJ*, 123, 1056
- Tegler, S. C., Romanishin, W., Consolmagno, G. J., et al. 2005, *Icarus*, 175, 390
- Thirouin, A., Ortiz, J. L., Duffard, R., et al. 2010, *A&A*, 522, A93
- Trilling, D. E., Hora, J. L., Mueller, M., et al. 2012, in *Asteroids, Comets, Meteors 2012*, *Proc. Conf. LPI Contribution*, 1667, 6485
- Trujillo, C. A., & Brown, M. E. 2002, *ApJ*, 566, L125
- Usui, F., Kasuga, T., Hasegawa, S., et al. 2013, *ApJ*, 752, 56
- Vilenius, E., Kiss, Cs., Mommert, M., et al. 2012, *A&A*, 541, A94
- Vilenius, E., Kiss, Cs., Müller, T., et al. 2013, *A&A*, submitted
- Werner, M. W., Roellig, T. L., Low, F. J., et al. 2004, *ApJS*, 154, 1

Table 3. Radiometric fit results.

Object	Data ¹	D [km]	p_v [%]	η	$r_h^{(2)}$	Class	Reference/Comment
Chariklo	P/W	235 ± 6	3.9 ^{+0.9} _{-0.7}	1.12 ^{+0.08} _{-0.08}	13.513	Centaur	(5)
Chiron	P/M	210 ⁺¹¹ ₋₁₀	17.6 ^{+4.0} _{-4.0}	0.91 ^{+0.09} _{-0.10}	14.872	Centaur	(5)
(145486) 2005 UJ ₄₃₈	P/M	16 ⁺¹ ₋₂	25.6 ^{+9.7} _{-7.6}	0.34 ^{+0.09} _{-0.08}	8.427	Centaur	(9)
Amycus	P/M	104 ± 8	8.3 ^{+1.6} _{-1.5}	1.00 ^{+0.12} _{-0.13}	16.248	Centaur	(9)
Asbolus	M	85 ⁺⁸ ₋₉	5.6 ^{+1.9} _{-1.5}	0.97 ^{+0.14} _{-0.18}	8.748	Centaur	(9)
Bienor	P/M	198 ⁺⁶ ₋₇	4.3 ^{+1.6} _{-1.2}	1.58 ^{+0.07} _{-0.07}	18.016	Centaur	(9)
Echeclus	P/M	64 ± 2	5.4 ^{+0.7} _{-0.6}	0.84 ± 0.04	10.861	Centaur	(9)
Hylonome	P/M	77 ± 15	4.8 ^{+2.7} _{-1.4}	1.34 ^{+0.31} _{-0.30}	20.933	Centaur	(9)
(136204) 2003 WL ₇	P/M	105 ⁺⁴ ₋₃	5.2 ^{+1.0} _{-0.7}	1.02 ^{+0.07} _{-0.05}	15.076	Centaur	(9)
Okyrhoe	P/M	35 ± 3	5.6 ^{+1.2} _{-1.0}	0.71 ^{+0.12} _{-0.13}	7.232	Centaur	(9)
Pholus	P/M	107 ⁺¹⁸ ₋₁₉	12.6 ^{+7.6} _{-4.9}	0.94 ^{+0.30} _{-0.28}	21.398	Centaur	(9)
Thereus	P/M	62 ± 3	8.3 ^{+1.6} _{-1.3}	0.87 ^{+0.08} _{-0.08}	10.948	Centaur	(9)
(95626) 2002 GZ ₃₂	P/M	237 ± 8	3.7 ^{+0.4} _{-0.4}	0.97 ^{+0.05} _{-0.07}	19.366	Centaur	(9)
(120061) 2003 CO ₁	P/M	94 ± 5	4.9 ^{+0.5} _{-0.6}	1.23 ^{+0.12} _{-0.11}	11.479	Centaur	(9)
2005 RO ₄₃	P/M	194 ± 10	5.6 ^{+3.6} _{-2.1}	1.12 ^{+0.05} _{-0.08}	25.954	Centaur	(9)
2006 SX ₃₆₈	P/M	76 ± 2	5.2 ^{+0.7} _{-0.6}	0.87 ^{+0.04} _{-0.06}	12.030	Centaur	(9)
(29981) 1999 TD ₁₀	M	104 ± 14	4.4 ^{+1.4} _{-1.0}	1.64 ^{+0.32} _{-0.31}	14.137	Centaur	(11)
(119951) 2002 KX ₁₄	P/M	455 ± 27	9.7 ^{+1.4} _{-1.3}	1.79 ^{+0.16} _{-0.15}	39.530	Classical	(3)
2001 RZ ₁₄₃	P/M	140 ⁺³⁹ ₋₃₃	19.1 ^{+6.6} _{-4.5}	0.75 ^{+0.23} _{-0.19}	41.327	Classical	(3)
Sila	P/M	343 ± 42	9.0 ^{+2.7} _{-1.7}	1.36 ^{+0.21} _{-0.19}	43.512	Classical	(3)
Teharonhiawako	P/M	177 ⁺⁴⁶ ₋₄₄	22.0 ⁺¹⁴ _{-8.0}	0.86 ^{+0.37} _{-0.29}	45.057	Classical	(3)
Makemake	S	1430 ± 9	77 ± 3	2.29 ^{+0.46} _{-0.40}	52.165	Classical	(10), D & p_v from occ. (see text)
Altjira	P/M	257 ⁺⁹⁰ ₋₉₂	7.1 ^{+4.9} _{-2.1}	1.46 ± 0.41	45.469	Classical	(3)
2001 KA ₇₇	P/M	310 ⁺¹⁷⁰ ₋₆₀	9.9 ^{+5.2} _{-5.6}	2.52 ^{+0.18} _{-0.83}	48.306	Classical	(3)
Chaos	P/M	600 ⁺¹⁴⁰ ₋₁₃₀	5.0 ^{+3.0} _{-1.6}	2.20 ^{+1.20} _{-1.10}	41.811	Classical	(3)
(307261) 2002 MS ₄	P/M	934 ± 47	5.1 ^{+3.6} _{-2.2}	1.06 ± 0.06	47.241	Classical	(3)
(90568) 2004 GV ₉	P/M	680 ± 34	7.7 ^{+0.8} _{-0.8}	1.93 ^{+0.09} _{-0.07}	39.122	Classical	(3)
(78799) 2002 XW ₉₃	P	565 ⁺⁷¹ ₋₇₃	3.8 ^{+4.3} _{-2.5}	0.79 ^{+0.27} _{-0.24}	44.627	Classical	(3)
Salacia	P/M	901 ± 45	4.4 ^{+0.4} _{-0.4}	1.16 ± 0.03	43.983	Classical	(3,5)
Haumea	P/S/M	1240 ⁺⁶⁹ ₋₅₉	80.4 ^{+6.2} _{-9.5}	0.95 ^{+0.33} _{-0.26}	51.062	Classical	(5)
Varuna	P/M	668 ⁺¹⁵⁴ ₋₈₆	12.7 ^{+4.0} _{-4.2}	2.18 ^{+1.04} _{-0.49}	43.231	Classical	This work
Borasisi	P/M	163 ⁺³² ₋₆₆	23.6 ^{+43.8} _{-7.7}	0.77 ^{+0.19} _{-0.47}	41.38	Classical	(8)
(55565) 2002 AW ₁₉₇	P/M	768 ⁺³⁹ ₋₃₈	11.2 ^{+1.2} _{-1.1}	1.29 ^{+0.10} _{-0.13}	46.520	Classical	(8)
Quaoar	P/M	1074 ± 38	12.7 ^{+1.0} _{-0.9}	1.73 ^{+0.08} _{-0.08}	43.224	Classical	(5)
(55637) 2002 UX ₂₅	P/M	697 ⁺²³ ₋₂₅	10.7 ^{+0.5} _{-0.8}	1.07 ^{+0.08} _{-0.05}	41.813	Classical	(5)
(55636) 2002 TX ₃₀₀	P/M	286 ± 10	88.0 ^{+15.0} _{-6.0}	1.15 ^{+0.55} _{-0.74}	41.204	Classical	This work, D & p_v from occ. (see text)
(230965) 2004 XA ₁₉₂	P	339 ⁺¹²⁰ ₋₉₅	26 ⁺³⁴ ₋₁₅	0.62 ^{+0.79} _{-0.49}	35.71	Classical	(8)
2004 NT ₃₃	P	423 ⁺⁸⁷ ₋₈₀	12.5 ^{+6.9} _{-3.9}	0.69 ^{+0.46} _{-0.32}	38.33	Classical	(8)
2004 PT ₁₀₇	P	330 ⁺¹¹⁰ ₋₁₀₀	4.8 ^{+5.2} _{-2.2}	0.85 ^{+0.91} _{-0.57}	38.30	Classical	(8)
2003 QA ₉₁	P/M	260 ⁺³⁰ ₋₃₆	13.0 ^{+11.9} _{-7.5}	0.83 ^{+0.10} _{-0.15}	44.72	Classical	(8)
2003 QR ₉₁	M	280 ± 28	1.8 ^{+1.7} _{-1.1}	1.23 ^{+0.10} _{-0.11}	39.12	Classical	(8)
2001 QC ₂₉₈	M	303 ⁺²⁹ ₋₃₂	6.3 ^{+2.8} _{-1.8}	0.983 ^{+0.10} _{-0.09}	40.62	Classical	(8)
(174567) 2003 MW ₁₂	P	792 ⁺⁹¹ ₋₈₄	10.2 ^{+2.4} _{-2.0}	0.84 ^{+0.28} _{-0.22}	47.62	Classical	(8)
2002 GJ ₃₂	M	224 ⁺⁸⁸ ₋₇₀	12 ⁺¹⁴ _{-6.0}	1.78 ^{+0.74} _{-0.60}	43.2	Classical	(12)
1996 TS ₆₆	M	194 ⁺⁵⁴ ₋₃₈	12 ^{+7.2} _{-4.7}	0.96 ^{+0.27} _{-0.18}	38.5	Classical	(12)
(120348) 2004 TY ₃₆₄	P/M	512 ⁺³⁷ ₋₄₀	10.7 ^{+2.0} _{-1.5}	1.55 ^{+0.15} _{-0.10}	39.543	Plutino	This work
(47171) 1999 TC ₃₆	P/M	393 ⁺²⁵ ₋₂₇	7.9 ^{+1.3} _{-1.1}	1.10 ^{+0.07} _{-0.08}	30.885	Plutino	(2)
(47932) 2000 GN ₁₇₁	P/M	147 ⁺²¹ ₋₂₈	21.5 ^{+9.3} _{-7.0}	1.11 ^{+0.24} _{-0.21}	28.396	Plutino	(2)
(55638) 2002 VE ₉₅	P/M	250 ⁺¹⁴ ₋₁₃	14.9 ^{+1.9} _{-1.6}	1.40 ^{+0.12} _{-0.11}	28.383	Plutino	(2)
2002 XV ₉₃	P/M	549 ⁺²² ₋₂₃	4.0 ^{+2.0} _{-1.5}	1.24 ± 0.06	39.862	Plutino	(2)
(208996) 2003 AZ ₈₄	P/M	727 ⁺⁶² ₋₆₇	10.7 ^{+2.3} _{-1.6}	1.05 ^{+0.19} _{-0.15}	45.445	Plutino	(2)

Notes. ⁽¹⁾ P = PACS; S = SPIRE, M = MIPS, W = WISE. ⁽²⁾ Mean heliocentric distance for the relevant observations.

References. (1) Santos-Sanz et al. (2012); (2) Mommert et al. (2012); (3) Vilenius et al. (2012); (4) Pál et al. (2012); (5) Fornasier et al. (2013); (6) Kiss et al. (2013a); (7) Kiss et al. (in prep.); (8) Vilenius et al. (in prep.); (9) Duffard et al. (in prep.); (10) Lim et al. (2010); (11) Stansberry et al. (2008); (12) Brucker et al. (2009).

Table 3. continued.

Object	Data ¹	D [km]	p_v [%]	η	r_h^2	Class	Reference/Comment
(84922) 2003 VS ₂	P/M	523 ⁺³⁵ ₋₃₄	14.7 ^{+6.3} _{-4.3}	1.57 ^{+0.30} _{-0.23}	36.458	Plutino	(2)
(120216) 2004 EW ₉₅	P	266 ⁺⁴⁸ ₋₄₅	5.3 ^{+3.5} _{-2.2}	0.93 ^{+0.55} _{-0.42}	27.471	Plutino	(2)
(175113) 2004 PF ₁₁₅	P	406 ⁺⁹⁸ ₋₈₅	11.3 ^{+8.2} _{-4.2}	0.84 ^{+0.61} _{-0.40}	41.427	Plutino	(2)
(144897) 2004 UX ₁₀	P	361 ⁺¹²⁴ ₋₉₄	17.2 ^{+14.1} _{-7.8}	0.96 ^{+0.98} _{-0.56}	38.950	Plutino	(2)
2006 HJ ₁₂₃	P	283 ⁺¹⁴² ₋₁₁₁	13.6 ^{+30.8} _{-8.9}	2.48 ^{+3.92} _{-1.91}	36.538	Plutino	(2)
Huya	P/M	459 ± 9	8.3 ± 0.4	0.93 ± 0.02	28.996	Plutino	(2,5)
Orcus	P/M	958 ± 24	23.7 ^{+1.2} _{-1.7}	0.98 ^{+0.05} _{-0.04}	47.839	Plutino	(5)
(15820) 1994 TB	P/M	85 ⁺³⁶ ₋₂₈	17.2 ^{+25.8} _{-9.7}	1.26 ^{+0.97} _{-0.65}	27.914	Plutino	This work
Ixion	P/M	617 ⁺¹⁹ ₋₂₀	14.1 ± 1.1	0.91 ^{+0.04} _{-0.06}	41.769	Plutino	This work
(33340) 1998 VG ₄₄	P/M	248 ⁺⁴³ ₋₄₁	6.3 ^{+2.6} _{-1.7}	1.55 ^{+0.58} _{-0.38}	29.478	Plutino	This work
(26308) 1998 SM ₁₆₅	P/M	291 ⁺²² ₋₂₆	8.3 ^{+1.8} _{-1.3}	1.55 ^{+0.11} _{-0.10}	36.970	Res 1:2	This work
(26375) 1999 DE ₉	P/M	311 ⁺²⁹ ₋₃₂	16.3 ^{+4.1} _{-2.6}	0.71 ^{+0.10} _{-0.11}	35.611	Res 2:5	This work
2002 TC302	P/M	584 ⁺¹⁰⁶ ₋₈₈	11.5 ^{+4.7} _{-3.3}	1.09 ^{+0.37} _{-0.25}	46.230	Res 2:5	(5)
(119979) 2002 WC ₁₉	P/M	348 ± 45	16.7 ^{+5.2} _{-3.7}	1.12 ^{+0.16} _{-0.17}	42.402	Res 1:2	This work
2001 QR ₃₂₂	M	132 ± 24	5.8 ^{+2.9} _{-1.6}	1.16 ^{+0.21} _{-0.22}	29.7	Res 1:1	(12)
(15874) 1996 TL ₆₆	P/M	338 ± 18	11.0 ^{+2.1} _{-1.5}	1.15 ^{+0.08} _{-0.05}	35.581	SDO	(1)
(82158) 2001 FP ₁₈₅	P/M	332 ⁺³¹ ₋₂₄	4.6 ± 0.7	1.23 ^{+0.24} _{-0.19}	34.596	SDO	(1)
(73480) 2002 PN ₃₄	P/M	112 ± 7	4.9 ± 0.6	1.02 ^{+0.07} _{-0.09}	16.059	SDO	(1)
(127546) 2002 XU ₉₃	P/M	164 ± 9	3.8 ± 0.5	1.12 ^{+0.05} _{-0.08}	21.098	SDO	(1)
Ceto	P/M	281 ± 11	5.6 ± 0.6	1.05 ± 0.05	29.826	SDO	(1)
Typhon	P/M	185 ± 7	4.4 ± 0.4	1.48 ± 0.07	17.947	SDO	(1)
(225088) 2007 OR ₁₀	P	1142 ⁺⁶⁴⁷ ₋₄₆₇	17.4 ^{+32.0} _{-10.4}	0.87 ^{+1.41} _{-0.70}	86.330	SDO	(1), refit with floating η
(309239) 2007 RW ₁₀	P	253 ⁺⁵⁰ ₋₅₂	6.6 ^{+6.6} _{-3.2}	1.26 ^{+0.82} _{-0.60}	27.456	SDO	(1), refit with floating η
2010 EK ₁₃₉	P	433 ⁺⁶³ ₋₆₄	29.7 ^{+11.3} _{-7.8}	0.60 ^{+0.33} _{-0.25}	39.080	SDO	Fluxes from (4), refit
(44594) 1999 OX ₃	P/M	135 ⁺¹³ ₋₁₂	8.1 ^{+1.8} _{-1.5}	1.04 ^{+0.27} _{-0.22}	23.083	SDO	This work
(48639) 1995 TL ₈	P/M	244 ⁺⁸² ₋₆₃	23.1 ^{+18.9} _{-10.2}	1.38 ^{+0.80} _{-0.49}	43.748	SDO	This work
(120132) 2003 FY ₁₂₈	P/M	461 ± 20	7.9 ± 1.0	1.07 ± 0.08	38.599	Detached	(1)
Sedna	P	906 ⁺³¹⁴ ₋₂₅₈	41.0 ^{+39.3} _{-18.6}	0.72 ^{+0.78} _{-0.54}	87.430	Detached	Fluxes from (4), refit
(145480) 2005 TB ₁₉₀	P	507 ⁺¹²⁷ ₋₁₁₆	12.1 ^{+8.8} _{-4.4}	1.44 ^{+0.95} _{-0.69}	46.377	Detached	(1), refit with floating η
2007 OC ₁₀	P	306 ⁺⁹³ ₋₇₂	13.0 ^{+9.5} _{-5.6}	1.17 ^{+1.11} _{-0.64}	35.516	Detached	(1), refit with floating η
Eris	P	2326 ± 12	96.0 ± 4	0.87 ^{+0.26} _{-0.41}	96.779	Detached	(7), D & p_V from occ. (see text)
2012 DR ₃₀	P/W	188 ± 7	7.7 ^{+2.8} _{-2.1}	0.81 ^{+0.08} _{-0.07}	14.51	Unknown	(6)
Phoebe	P/M	213 ± 1.4	8.2 ^{+0.2} _{-0.2}	1.32 ^{+0.03} _{-0.04}	9.338	Saturn moon	This work, fixed D & p_V (see text)
Sycorax	P	165 ⁺³⁶ ₋₄₂	4.9 ^{+3.8} _{-1.7}	1.26 ^{+0.92} _{-0.78}	20.084	Uranus moon	This work